



Key Points:

- Deep Argo trajectories trace the deep western boundary current (DWBC) pathway, including recirculation over the Kermadec Trench
- The deep salinity maximum is eroded as the DWBC exits the Kermadec Trench to the north through the Louisville Seamount Chain collision zone
- Seasonal heaving in the northern Kermadec Trench is predominantly driven by local Ekman pumping at the surface

Supporting Information:

Supporting Information may be found in the online version of this article.

Correspondence to:

M. Chandler,
mlchandler@ucsd.edu

Citation:

Chandler, M., Zilberman, N. V., & Sprintall, J. (2024). The deep western boundary current of the Southwest Pacific Basin: Insights from Deep Argo. *Journal of Geophysical Research: Oceans*, 129, e2024JC021098. <https://doi.org/10.1029/2024JC021098>

Received 7 MAR 2024

Accepted 7 OCT 2024

Author Contributions:

Conceptualization: Mitchell Chandler, Nathalie V. Zilberman, Janet Sprintall

Data curation: Mitchell Chandler

Formal analysis: Mitchell Chandler

Funding acquisition: Nathalie V. Zilberman, Janet Sprintall

Methodology: Mitchell Chandler, Nathalie V. Zilberman, Janet Sprintall

Project administration:

Mitchell Chandler

Resources: Nathalie V. Zilberman, Janet Sprintall

Software: Mitchell Chandler

Supervision: Nathalie V. Zilberman, Janet Sprintall

Validation: Mitchell Chandler

© 2024. The Author(s).

This is an open access article under the terms of the Creative Commons

Attribution License, which permits use, distribution and reproduction in any medium, provided the original work is properly cited.

The Deep Western Boundary Current of the Southwest Pacific Basin: Insights From Deep Argo

Mitchell Chandler¹ , Nathalie V. Zilberman¹ , and Janet Sprintall¹ 

¹Scripps Institution of Oceanography, University of California San Diego, La Jolla, CA, USA

Abstract The deep western boundary current (DWBC) of the Southwest Pacific Basin (SWPB) is the main pathway through which the deep and bottom waters formed around Antarctica are transported northward and distributed throughout the Pacific Ocean. However, historical observations of this current are sparse. Here, we used an unprecedented number of deep-ocean observations collected by Deep Argo floats since 2016 to examine temperature, salinity, and velocity in the DWBC of the SWPB. Deep Argo trajectory velocities were fastest along the western side of the Kermadec Trench, with an average velocity of $0.057 \pm 0.012 \text{ m s}^{-1}$. Trajectories confirmed the existence of a tight recirculation on the eastern side of the Kermadec Trench ($-0.021 \pm 0.008 \text{ m s}^{-1}$). This recirculation was likewise seen in an independent eddy-resolving ocean reanalysis. For the DWBC within the northern Kermadec Trench ($26\text{--}30^\circ\text{S}$), Deep Argo profiles and the ocean reanalysis demonstrated seasonal isopycnal heaving of the deep-ocean that was likely driven by local Ekman pumping and may influence seasonal DWBC transport. At the northern end of the Kermadec Trench, the deep-ocean salinity maximum was eroded as the DWBC exited the trench to the north through the Louisville Seamount Chain collision zone, thus revealing a previously unidentified region of enhanced deep-ocean mixing. Although Deep Argo observations accurately estimated vertical turbulent diffusivity in the Samoan Passage (6.1×10^{-3} to $1.57 \times 10^{-2} \text{ m}^2 \text{ s}^{-1}$), mixing within the Louisville Seamount Chain collision zone was not due solely to vertical turbulent diffusivity. A global Deep Argo array could reveal wind-driven seasonal heaving and unexplored deep-ocean mixing hotspots in other DWBCs.

Plain Language Summary The cold and dense seawater that fills the ocean interior is formed near the surface in polar regions. This seawater sinks and is transported away from the poles and throughout the ocean by deep western boundary currents. We used data collected by Deep Argo floats (freely drifting robots that measure temperature and salinity between the sea surface and seafloor) to examine the northward-flowing deep western boundary current in the Southwest Pacific Ocean, north-east of New Zealand. The pathway and speed of the current was identified using the horizontal movements of these floats. A clockwise circulation was evident over a deep-ocean trench (the Kermadec Trench), with some of the current's northward-flow returning southward. At the northern end of the Kermadec Trench, temperature and salinity demonstrated seasonal changes that extended at least 4,000-m deep. These seasonal changes were likely caused by seasonal changes in surface winds, and may influence seasonal transport of water in the deep western boundary current. Saltier waters observed over the Kermadec Trench were not observed north of the trench, identifying the exit of the Kermadec Trench as a region of enhanced deep-ocean mixing. Implementing Deep Argo globally could reveal other unidentified regions of enhanced deep-ocean mixing.

1. Introduction

The Deep Western Boundary Currents (DWBCs) of the Southern Hemisphere are major ocean currents located on the western side of deep-ocean basins (e.g., Fukamachi et al., 2010; Purkey & Johnson, 2012; Stommel & Arons, 1959b; Warren, 1981; Whitworth III et al., 1991, 1999). These DWBCs are the main conduit through which cold, dense water is transported away from Antarctica, filling the deep and abyssal ocean (Johnson, 2008; Stommel & Arons, 1959a). DWBCs are therefore a critical component of the lower cell of the meridional overturning circulation that redistributes heat, salt, carbon, nutrients, and oxygen (Sloyan et al., 2013; Talley, 2013). Changes in deep and bottom water properties, due to climatic changes at high-latitude formation regions, are advected by these DWBCs, impacting climate variability (Purkey & Johnson, 2010, 2013; Purkey et al., 2019), dissolved oxygen content (Gunn et al., 2023; Sloyan et al., 2013), and steric expansion and sea level (Desbruyères et al., 2016; Kouketsu et al., 2011; Purkey & Johnson, 2010, 2013; Purkey et al., 2019).

Visualization: Mitchell Chandler

Writing – original draft:

Mitchell Chandler

Writing – review & editing:

Mitchell Chandler, Nathalie V. Zilberman,
Janet Sprintall

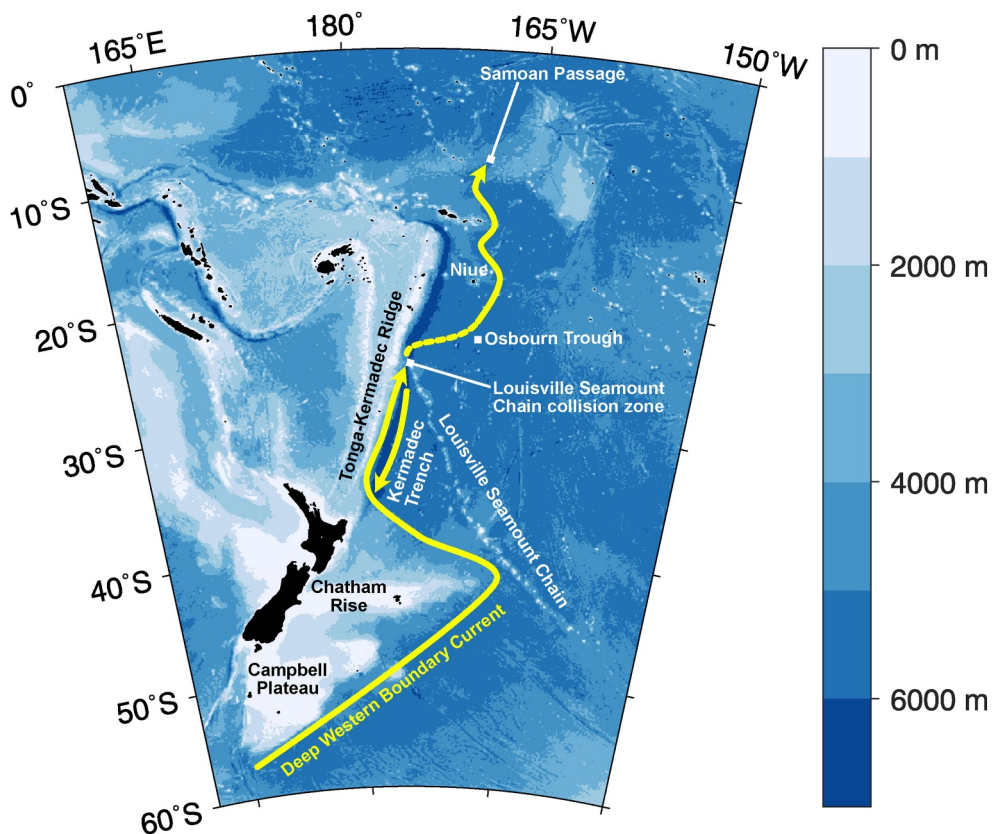


Figure 1. Bathymetry at the western boundary of the Southwest Pacific Basin with a schematic of the deep western boundary current pathway (yellow, dashed line represents an uncertain pathway). Key bathymetric features are labeled.

Many studies of the deep-ocean have used shipboard measurements, such as those from quasi-decadal repeat hydrographic surveys (Sloyan et al., 2019). Yet observations of the deep-ocean are limited, with less than 10% of historical non-Argo temperature and salinity profiles extending below 2,000-dbar (Roemmich et al., 2021). Such sparse measurements mean that DWBCs are one of the least observed large-scale circulation features in the global ocean. The recent implementation of Deep Argo floats that measure temperature, salinity, and pressure as they profile between the sea surface and as deep as 6,000-dbar has afforded a new way of studying the deep-ocean (Roemmich, Alford, et al., 2019; Roemmich, Sherman, et al., 2019; Zilberman, Thierry, et al., 2023). However, the spatial coverage of Deep Argo is presently restricted to a small number of regional pilot arrays (e.g., Desbruyères et al., 2022; Johnson, 2022; Johnson et al., 2019, 2020; Petit et al., 2022; Racapé et al., 2019; Thomas et al., 2020; Zilberman et al., 2020).

This work is focused on the Southwest Pacific Basin (SWPB), the location of one of the pilot arrays that has been most densely sampled by Deep Argo floats. Historical studies have suggested that the DWBC of the SWPB (Figure 1) flows equatorward along the Campbell Plateau, around the Chatham Rise, and through the Kermadec Trench (Reid, 1986, 1997). The main DWBC pathway then becomes less clear, although the majority of flow appears to divert eastward (Warren & Voorhis, 1970). Eventually, the DWBC exits the SWPB to the north, predominantly through the Samoan Passage (Roemmich et al., 1996). Velocities within the DWBC have been measured to be bottom-intensified in both the Kermadec Trench (Whitworth III et al., 1999) and Samoan Passage (Alford et al., 2013; Rudnick, 1997; Voet et al., 2015, 2016).

As there are no deep-water formation sites in the North Pacific Ocean, the SWPB DWBC is the main pathway by which the deep and bottom waters formed around Antarctica make their way into the western South Pacific Ocean and North Pacific Ocean (Johnson, 2008; Talley, 2013). Specifically, this DWBC transports high oxygen and low nutrient Lower Circumpolar Deep Water (Whitworth III et al., 1999; Wijffels et al., 2001). In the SWPB, Lower Circumpolar Deep Water is composed primarily of relatively cold and fresh Antarctic Bottom Water, although a

salinity maximum at shallower levels (depths of approximately 3,000–4,000-m at 32.5°S) reflects the influence of remnant North Atlantic Deep Water (NADW; Figure 2; Whitworth III et al., 1999; Johnson, 2008; Wijffels et al., 2001). Above the Lower Circumpolar Deep Water lies a return flow of warmer, fresher, lower oxygen, and higher nutrient Pacific Deep Water (Whitworth III et al., 1999; Wijffels et al., 2001).

Whitworth III et al. (1999) measured the SWPB DWBC over 1991–1992 using a mooring array at 32.5°S and found a time-mean transport of 16.0 Sv ($1 \text{ Sv} \equiv 1 \times 10^6 \text{ m}^3 \text{ s}^{-1}$) below 2,000-m. Transport variability was large (standard deviation of 11.9 Sv), with dominant periods of variability between 40 to 100-day (Whitworth III et al., 1999). This large variability may be due to the influence of Rossby waves at the western boundary of the SWPB (Moore & Wilkin, 1998). Further north, in the Samoan Passage, time-mean transport below 4,000-m has been estimated from mooring arrays to be 6.0 ± 0.5 Sv during 1992–1994 (Roemmich et al., 1996; Rudnick, 1997) and 5.4 ± 0.6 Sv during 2012–2013 (Voet et al., 2016). Both time series demonstrated large variability at tidal frequencies and sporadically at roughly 30-day periods, which may be related to resonance of the flow (Rudnick, 1997). Roemmich et al. (1996) combined observations from the 1992–1994 mooring array with a full-depth hydrographic survey in 1994 to estimate a total mean northward transport out of the SWPB (including the Samoan Passage and other smaller transport pathways) of 10.6 ± 1.7 Sv relative to the 1.2°C potential temperature (θ) surface. Transport out of the SWPB was therefore less than that measured by Whitworth III et al. (1999) in the DWBC at 32.5°S. At least part of this transport discrepancy is likely due to a broad return flow within the interior of the SWPB between 1,800 and 4,100-dbar (Zilberman et al., 2020).

Earlier studies have also hinted at a tight cyclonic circulation over the Kermadec Trench, consisting of the strong equatorward-flowing DWBC on the western flank and a weaker poleward-flowing recirculation on the eastern flank (Johnson, 1998). Evidence for this recirculation has been largely based on hydrographic and velocity measurements at the 32.5°S mooring array, where time-mean meridional velocities on the eastern side of the trench were small but southward (on the order of -0.01 m s^{-1} ; Whitworth III et al., 1999). A hydrographic survey at 28°S also suggested the presence of southward flow on the eastern side of the trench (Warren, 1973), but the spatial extent of this recirculation is unresolved due to sparse historical observations. As yet, it is unknown whether the southward velocities on the eastern side of the Kermadec Trench are part of a cyclonic circulation that spans the entire trench.

As the DWBC exits the SWPB through the Samoan Passage, a large volume of water is forced over the complex bathymetry and series of sills (Alford et al., 2013). Vertical (or diapycnal) turbulent diffusivity in the Samoan Passage is therefore significantly larger than background levels in the deep-ocean ($1 \times 10^{-5} \text{ m}^2 \text{ s}^{-1}$; Toole et al., 1994) and the canonical basin-scale average ($1 \times 10^{-4} \text{ m}^2 \text{ s}^{-1}$; Munk, 1966). Indeed, Roemmich et al. (1996) estimated diapycnal diffusivity in the Samoan Passage to be between 5×10^{-3} and $5 \times 10^{-2} \text{ m}^2 \text{ s}^{-1}$ below 0.7°C . More recently, Voet et al. (2015) estimated vertical turbulent diffusivities in the Samoan Passage of between 3×10^{-3} and $5 \times 10^{-2} \text{ m}^2 \text{ s}^{-1}$ averaged at the depth of the salinity maximum, and around $6 \times 10^{-3} \text{ m}^2 \text{ s}^{-1}$ below 0.8°C . However, turbulent mixing within the Samoan Passage is spatially heterogeneous (Alford et al., 2013; Voet et al., 2015), with diapycnal diffusivities as large as $1 \times 10^{-1} \text{ m}^2 \text{ s}^{-1}$ measured over the sills (Alford et al., 2013). This elevated deep-ocean turbulence mixes away the coldest and densest waters, erodes the higher salinities evident at the passage entrance, and thus sets the water mass properties of the abyssal North Pacific Ocean (Alford et al., 2013; Voet et al., 2015). We suspect there could be other such regions along the path of the SWPB DWBC where turbulent mixing is elevated, however, to the best of our knowledge, no specific locations have been identified.

Additionally, Deep Argo observations from the interior of the SWPB have suggested the presence of deep-ocean dynamic height (DH) seasonal cycles (Zilberman et al., 2020). These seasonal cycles differed between the subtropics (15–32°S) and mid-latitudes (32–46°S), and were hypothesized to be driven by regional Ekman pumping within the SWPB (Zilberman et al., 2020). It is unclear whether similar seasonal cycles occur in the DWBC as, at the time of Zilberman et al. (2020)'s study, there was insufficient Deep Argo coverage at the western boundary. Whitworth III et al. (1999) found no evidence of a seasonal cycle in DWBC transport at the 32.5°S mooring array, although the array was only deployed for 22-month. Furthermore, the array was located within the latitude range where the Ekman pumping seasonal cycle changes sign. Hence, if there is a DWBC seasonal cycle forced by Ekman pumping, it would likely not be evident at 32.5°S. Measurements from mooring arrays in the Samoan Passage have also been inconclusive as to the presence of a seasonal cycle, with wavelet spectra of

bottom water transport hinting at energy at the annual period (Voet et al., 2016), but again the short time series (17-month in the 1990s, 15-month in the 2010s) make determination of any seasonal cycle difficult.

Continued Deep Argo deployments in the SWPB have increased coverage of the western boundary in recent years. This blossoming data set can now be leveraged to provide new insights that were not previously feasible using sparse historical observations. In the present study we have examined flow pathways, turbulent mixing, and seasonality in the DWBC of the SWPB using 964 Deep Argo profiles and 711 Deep Argo trajectories collected since 2016. These observations allowed us to trace the path of the DWBC and, for the first time, clearly show the cyclonic recirculation over the entire Kermadec Trench. Deep Argo profiles revealed that the remnant NADW salinity maximum is eroded as the DWBC exits the Kermadec Trench to the north, marking the Louisville Seamount Chain collision zone as a previously unidentified deep-ocean mixing hotspot. We found seasonal isopycnal heaving in the northern Kermadec Trench, and suggest this deep-ocean heaving is forced by the local Ekman pumping seasonal cycle at the surface. In the remainder of this paper we outline the data and methods used (Section 2), present our results (Section 3), and discuss their implications (Section 4).

2. Data and Methodology

2.1. Deep Argo Profiles and Trajectories

Data were collected by 10 Deep Argo floats profiling within the DWBC of the SWPB (Figure 3). All floats were the Deep SOLO model capable of profiling down to 6,000-dbar (Roemmich, Sherman, et al., 2019). Following initial diagnostic cycles on deployment (Roemmich, Sherman, et al., 2019), these floats were set to 10-day or 15-day profiling cycles. Only delayed-mode profiles with adjusted temperature, salinity, and pressure flagged as “good” or “probably good” (Wong et al., 2022) were used in this study. Profiles shallower than 2,000-dbar or outside of the latitudinal range 5–40°S were excluded, which resulted in a total of 964 profiles since June 2016 with the most recent delayed-mode profile from January 2023. As the vertical resolution within and between float profiles varied (from near-continuous to 60-dbar), all profiles were linearly interpolated to a 10-dbar pressure grid (e.g., Foppert et al., 2021; Johnson et al., 2020). Temperature was converted to θ (relative to the sea surface, i.e. 0-dbar).

Deep Argo has target accuracies of ± 3 -dbar for pressure, $\pm 0.001^\circ\text{C}$ for temperature, and ± 0.002 PSS-78 for salinity (Roemmich, Alford, et al., 2019). Efforts are ongoing to achieve these targets, with prior observations indicating that the SBE-61 CTDs carried by Deep SOLO floats have accuracies of ± 4.5 -dbar for pressure, $\pm 0.001^\circ\text{C}$ for temperature, and ± 0.005 for salinity (Roemmich, Alford, et al., 2019). A compressibility correction of the conductivity cell that improves salinity accuracy to ± 0.002 (Foppert et al., 2021; Zilberman, Thierry, et al., 2023) was applied to the delayed-mode profiles here.

The Scripps Argo Trajectory-Based Velocity Product provides trajectories for all delayed-mode quality-controlled Argo floats with parking pressures between 100 and 6,200-dbar and profiling cycles between 5 and 25-day over the period 2001–2022 (Zilberman, Scanderbeg, et al., 2023a). These subsurface trajectory velocities were computed based on the float's drift distance and duration each profiling cycle (Zilberman, Scanderbeg, et al., 2023a). This product was used to obtain trajectories for the 10 Deep Argo floats in the DWBC. Most of the 711 Deep Argo trajectories (at time of writing, the product did not contain delayed-mode trajectories for floats 5906417, 5906419, or 5906420) were from floats parked at pressures around 5,000-dbar (75% were between 4,500 and 5,500-dbar). The shallowest trajectory parking pressure was 2,520-dbar and the deepest was 5,909-dbar.

2.2. Ocean Reanalysis

The $1/12^\circ$ Global Ocean Physics Reanalysis (GLORYS12V1, hereafter GLORYS; Lellouche et al., 2021) was used for comparison with Deep Argo profiles of temperature and salinity and Deep Argo subsurface trajectory velocities in the Kermadec Trench. GLORYS assimilates reprocessed and quality-controlled satellite observations of sea level anomaly, sea surface temperature, and sea ice concentration, as well as in situ observations of temperature and salinity (Lellouche et al., 2021). Deep Argo observations are not yet included in the reanalysis, with (non-Argo) climatological temperature and salinity assimilated below 2,000-m (Lellouche et al., 2018). As such, the Deep Argo and GLORYS data used here are independent of each other.

GLORYS can be used to examine variability from meso-scale to global-scale over time periods from days to decades (Lellouche et al., 2021). Previously, Song et al. (2023) used GLORYS to examine seasonality in the southward-flowing Philippine Trench DWBC and found that GLORYS successfully reproduced velocity variability, albeit with stronger velocities than observed. Here, monthly means of GLORYS θ and salinity between depths of 1,940 and 5,730-m and in the region bounded by 25–40°S, 179–185°E were downloaded for the period 1993–2020. The GLORYS time series therefore had limited overlap with the period of Deep Argo observations. Nevertheless, Deep Argo profiles and GLORYS θ and salinity profiles (time-averaged for the month in which the corresponding Deep Argo profile was measured) were similar (Figure 4). Although, compared to Deep Argo observations, GLORYS underestimated the salinity maximum, overestimated salinity in the coldest waters, and had colder bottom waters. GLORYS zonal and meridional velocities at 5,275-m (the depth level closest to the largest number of Deep Argo trajectory parking pressures) were also downloaded for the same time period and region.

2.3. Ekman Pumping

Monthly ERA5 (Hersbach et al., 2020) wind stress was downloaded for 1993–2020, the same time period as GLORYS, and used to compute Ekman pumping (w_{Ek}):

$$w_{Ek} = \frac{\frac{\partial \tau^y}{\partial x} - \frac{\partial \tau^x}{\partial y}}{\rho_0 f} \quad (1)$$

where τ^y is meridional wind stress, τ^x is zonal wind stress, x is zonal distance, y is meridional distance, ρ_0 is a representative surface density (1025 kg m⁻³), and f is the Coriolis parameter (e.g., Cushman-Roisin & Beckers, 2011). Ekman pumping seasonal cycles were obtained by least-squares fitting annual and semi-annual harmonics and a mean, then subtracting the fitted mean.

2.4. Turbulent Mixing

Vertical turbulent diffusivity (κ_z) was examined in the Samoan Passage and in the Louisville Seamount Chain collision zone. These two locations are bathymetric choke-points along the path of the DWBC (Figure 1) where substantial changes in water mass properties were observed (Figure 2). To estimate κ_z , the equation for conservation of a tracer C (either θ or salinity), with no sources or sinks, small aspect ratio (vertical scale much smaller than horizontal scale), horizontal changes only in the along-flow direction (no x -direction terms), and constant vertical turbulent diffusivity was used (e.g., Ffield & Gordon, 1992; Salmon, 1998; Voet et al., 2015).

In a reference frame moving with the flow, the conservation equation becomes (Ffield & Gordon, 1992):

$$\frac{\partial C}{\partial t} = \kappa_z \frac{\partial^2 C}{\partial z^2} \quad (2)$$

where t is time and z is depth. Following Voet et al. (2015), Equation 2 was applied to the mean θ and salinity profiles immediately upstream (within 2.7° of latitude) of each region and solved numerically using forward differencing. In the Samoan Passage, C was held constant at 3,600-m and a no flux boundary condition applied at the bottom. In the Louisville Seamount Chain collision zone, C was held constant at both 2,400 and 3,800-m. Model results depend on the spreading scale parameter $\lambda = \sqrt{\kappa_z t^*}$, where $t^* = \frac{y}{v}$ is the transit time through the choke-point with y the distance between the mean location of downstream and upstream profiles and v the mean Deep Argo trajectory velocity within the choke-point. Here, λ was taken to be the value that minimized the difference between the modeled θ -salinity profile and the mean profile observed downstream.

In a stationary reference frame and assuming a steady-state, the conservation equation instead becomes:

$$v \frac{\partial C}{\partial y} = \kappa_z \frac{\partial^2 C}{\partial z^2} \quad (3)$$

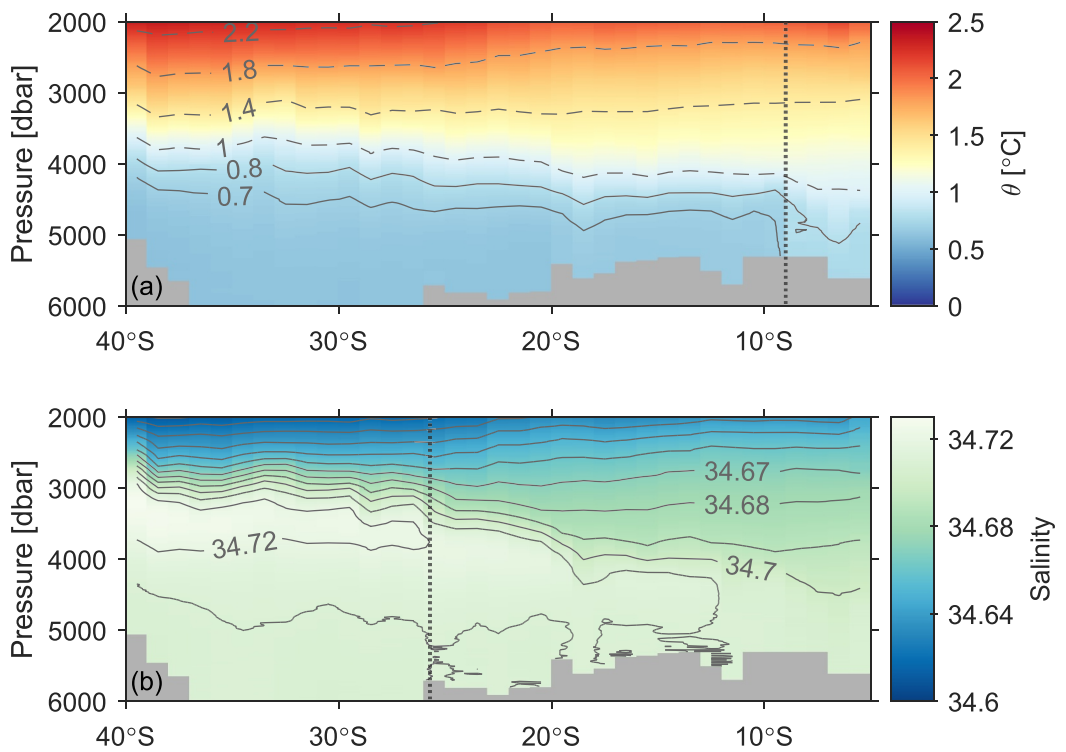


Figure 2. Meridional sections of (a) potential temperature (θ) and (b) salinity between 2,000 and 6,000-dbar from 1° zonal averages of Deep Argo profiles collected at the western boundary of the Southwest Pacific Basin between June 2016–January 2023 (see Figure 3 for profile locations and times). Vertical dotted lines mark the latitude of the (a) Samoan Passage (~9°S) and (b) Louisville Seamount Chain collision zone (~26°S).

Three of the terms in Equation 3 ($v, \frac{\partial C}{\partial y}, \frac{\partial^2 C}{\partial z^2}$) could be obtained from Deep Argo observations, allowing κ_c to be computed from direct observations. This calculation was only performed in the Samoan Passage, where the numerical model (Equation 2) reproduced a θ -salinity profile exceptionally similar to the mean observed downstream profile (Figure S1 in Supporting Information S1). Each term in Equation 3 was averaged below

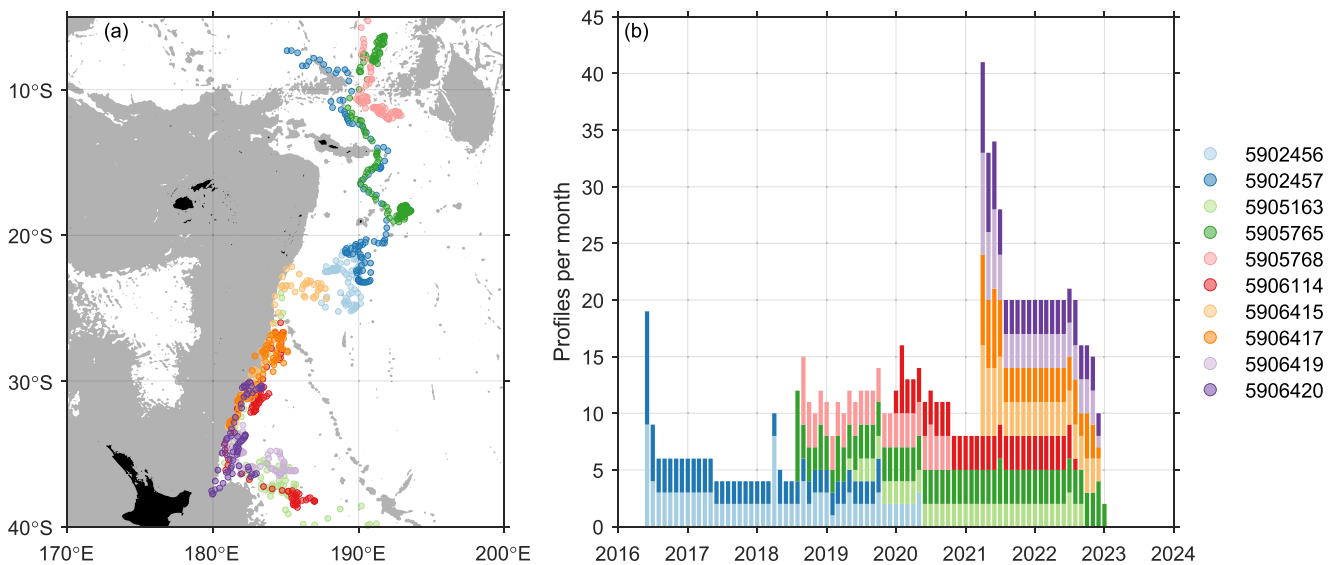


Figure 3. (a) Locations of Deep Argo profiles and (b) number of Deep Argo profiles per month, both colored according to float WMO identification number. Gray shading is bathymetry shallower than 4,000-m.

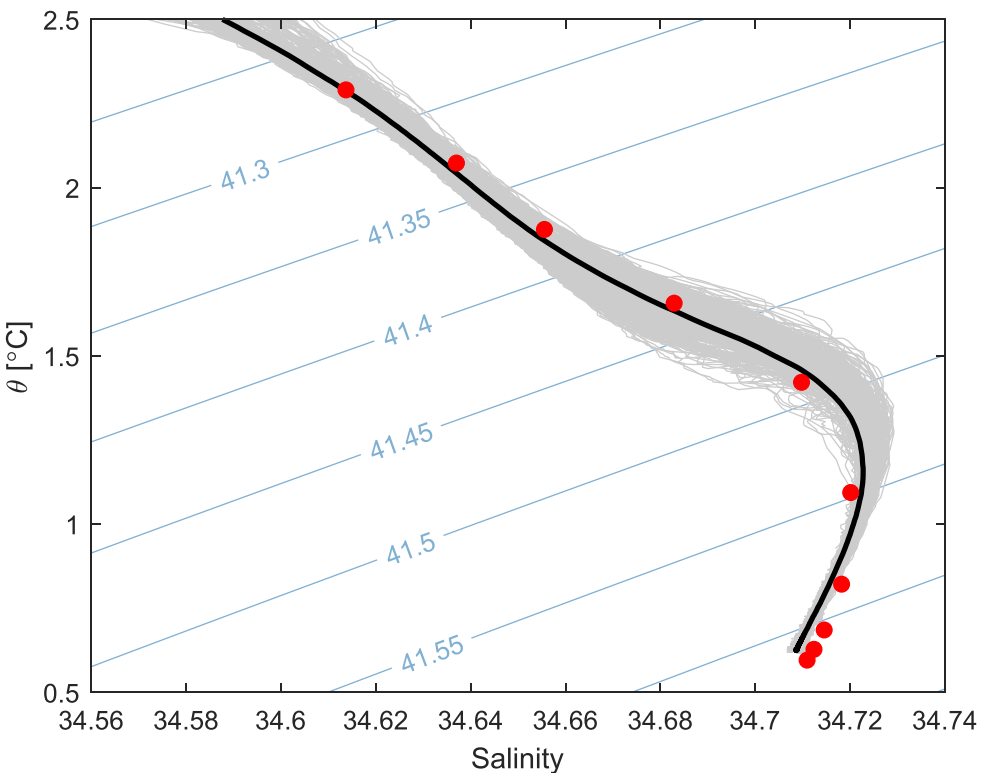


Figure 4. Potential temperature (θ)–salinity curves for all Deep Argo profiles in the Kermadec Trench (gray lines), the spatial-average of these Deep Argo profiles (black line), and the spatial-average of the GLORYS profiles interpolated to the locations of the Deep Argo profiles (red dots), with σ_3 (potential density anomaly referenced to 3,000-dbar; kg m^{-3}) contours in blue. Each GLORYS profile was the 1993–2020 time-average for the month in which the corresponding Deep Argo profile (December 2019–December 2022) was measured.

4,000-dbar (about 1.1°C), where the observed θ -salinity curves upstream and downstream of the Samoan Passage diverged, and κ_z was computed for both salinity and θ observations. The calculation was not performed in the Louisville Seamount Chain collision zone as the modeled profile evolution did not match the mean θ -salinity profile observed downstream (Figure S2 in Supporting Information S1), indicating that additional mixing processes other than just κ_z are important.

For both the numerical model and direct calculation, a bootstrapping approach was employed to compute 95% confidence intervals. Mean profiles, locations, and velocities were recomputed by sampling with replacement, and κ_z was recalculated using these new values. This procedure was repeated 1×10^4 times and the 2.5th and 97.5th percentile values of κ_z taken to represent the 95% confidence interval.

2.5. Seasonality

Deep Argo profiles in the DWBC along the Kermadec Trench were used to examine θ , salinity, and DH seasonal cycles in the deep-ocean. These profiles were identified using Deep Argo trajectories to select a region that encompassed just the northward flow on the western side of the trench (between 26 – 38°S). Profiles were spatially averaged each month to produce monthly time series for 2021–2022. To obtain seasonal cycles, annual and semi-annual harmonics and a mean were least-squares fit to the monthly time series. The mean was then subtracted from the least-squares fit. Seasonal cycles were computed between 2,000 and 4,000-dbar as 80% of profiles considered reached at least 4,000-dbar. DH was thus computed relative to 4,000-dbar and the 20% of profiles that did not reach 4,000-dbar were excluded. No profiles were excluded from the θ and salinity seasonal cycles. As such, the number of profiles contributing to the spatial-average each month ranged from 3 to 26 (average of 8.8 profiles) for θ and salinity, and from 0 to 15 (average of 7.0, with 0 profiles only occurring for 1 month) for DH. Observed θ , salinity, and DH seasonal signals were larger than Deep Argo measurement accuracies (± 0.002 for

salinity, $\pm 0.001^\circ\text{C}$ for temperature, $\pm 4.5\text{-dbar}$ for pressure, and $\pm 0.043 \text{ m}^2 \text{ s}^{-2}$ for DH at 2,000-dbar relative to 4,000-dbar).

To examine the cause of deep-ocean seasonality, the θ seasonal cycle was decomposed into heave (θ'_{heave} , i.e. changes on pressure surfaces due to isopycnal displacement) and spice (θ'_{spice} , i.e. changes on isopycnal surfaces due to water mass property changes) components (Bindoff & McDougall, 1994; Desbruyères et al., 2022; Häkkinen et al., 2015):

$$\theta' = \underbrace{\theta'|_\rho}_{\theta'_{\text{spice}}} + \underbrace{\frac{d\theta}{dp} p'|_\rho}_{\theta'_{\text{heave}}} \quad (4)$$

where p is pressure, and $X'|_\rho$ means the seasonal cycle of X on an isopycnal. Following Desbruyères et al. (2022), a σ_3 (potential density anomaly referenced to 3,000-dbar) vertical grid was constructed encompassing the depth range 2,000 to 4,000-dbar. For the spice component, θ was linearly interpolated onto the σ_3 grid and θ'_{spice} computed. For the heave component, $\frac{d\theta}{dp}$ and p were linearly interpolated onto the σ_3 grid and $p'|_\rho$ was multiplied by the $\frac{d\theta}{dp}$ seasonal cycle (with mean retained) to obtain θ'_{heave} . Both θ'_{spice} and θ'_{heave} were linearly interpolated back to the original pressure grid. The coefficient of determination (R^2) was used to evaluate the contribution of each term to the total θ seasonal cycle.

Seasonality was also computed using GLORYS interpolated to the locations of the Deep Argo profiles. The procedure was much the same as for Deep Argo, but every location had monthly θ , salinity, and DH over 1993–2020. Therefore, after spatial-averaging, time series were detrended before seasonal cycles were computed. Additionally, as local w_{Ek} seasonal cycles changed sign within the meridional range of the Kermadec Trench, GLORYS was used to compute seasonal cycles of θ , salinity, and DH along the DWBC in northern (26–30°S) and southern (32–36°S) trench regions.

3. Results

3.1. Deep Western Boundary Current Pathway

Deep Argo float trajectories illustrated the path of the DWBC through the SWPB in unprecedented detail (Figure 5). Beginning at 40°S, trajectories were northwest along the northern flank of the Chatham Rise (see Figure 1 for locations of bathymetric features) until reaching the Tonga-Kermadec Ridge, at which point they turned equatorward alongside the ridge. A clear recirculation of flow was evident over the Kermadec Trench, with poleward trajectories along the eastern side of the trench (Figure 5b). Continuing equatorward, trajectories exited the Kermadec Trench through the Louisville Seamount Chain collision zone. Trajectory directions were incoherent within the Osbourn Trough, suggesting the DWBC may break up into an eddy field here. On the northern side of the trough, around the latitude of Niue, trajectories re-coalesced into a coherent equatorward flow approximately following the 5,000-m isobath before exiting the SWPB through the Samoan Passage (Figure 5c).

Trajectory velocities within the two coherent regions of equatorward flow were stronger in the Kermadec Trench than between Niue and the Samoan Passage, with an average velocity (over all parking pressures) of $0.057 \pm 0.012 \text{ m s}^{-1}$ (95% confidence interval computed using a bootstrapping approach) compared to $0.031 \pm 0.005 \text{ m s}^{-1}$. The poleward-flowing recirculation over the Kermadec Trench ($-0.021 \pm 0.008 \text{ m s}^{-1}$) was also weaker than the equatorward-flowing DWBC. The average velocity in the Samoan Passage was $0.020 \pm 0.010 \text{ m s}^{-1}$. Deep Argo trajectories were the same order of magnitude and consistent in direction with time-mean velocities from moored current meters at PCM9 in the Kermadec Trench over February 1991–December 1992 (Figure 5b; Whitworth III et al., 1999) and PCM11 in the Samoan Passage over September 1992–February 1994 (Figure 5c; Rudnick, 1997).

The Kermadec Trench DWBC and recirculation were also present in an eddy-resolving ocean reanalysis. GLORYS time-mean velocities over 1993–2020 at 5,275-m depth demonstrated strong equatorward velocities on the western side of the trench and weaker poleward velocities on the eastern side (Figure 6a), qualitatively similar to Deep Argo trajectory velocities over 2021–2022 (Figures 5b and 6b). However, GLORYS tended to overestimate speed in the southern Kermadec Trench and underestimate speed in the northern Kermadec Trench

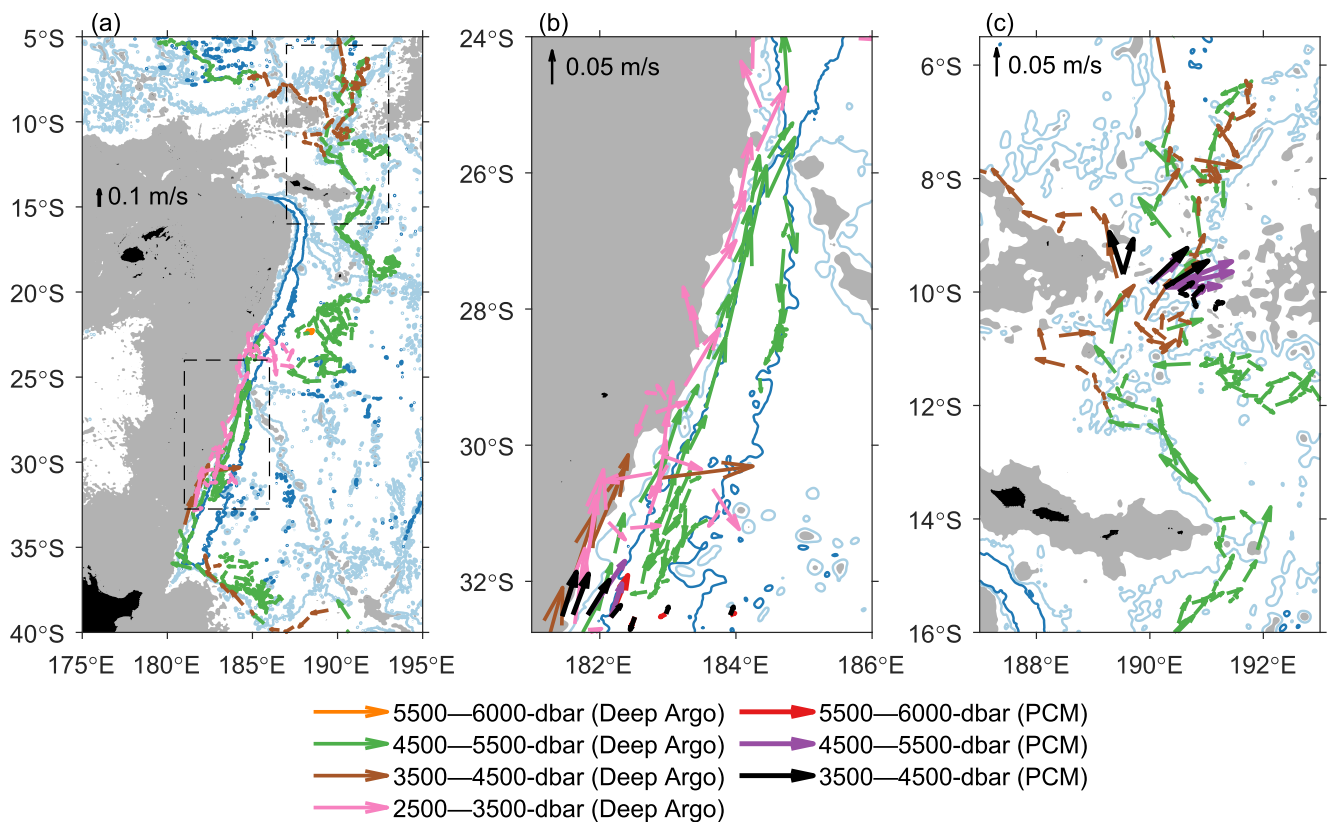


Figure 5. (a) Deep Argo trajectory velocities (July 2016–December 2022) in the deep western boundary current of the Southwest Pacific Basin. Dashed boxes in (a) are presented in the following panels with Deep Argo trajectory velocities and historical time-mean velocities from WOCE mooring array (b) PCM9 (February 1991–December 1992) in the Kermadec Trench and (c) PCM11 (September 1992–February 1994) in the Samoan Passage. Velocities are grouped by depth (parking pressure for Deep Argo, instrument depth for mooring arrays). Note the 5,500 to 6,000-dbar Deep Argo trajectories are small and only located near 22°S. Bathymetry contours are 5,000-m (light blue) and 6,000-m (dark blue), gray shading is shallower than 4,000-m.

(Figures 6b and 6c). This discrepancy in speed moving along the trench could be due to semi-permanent eddies or smaller recirculation features that were evident in the GLORYS time-mean DWBC velocity field (e.g., between roughly 35.2–34.4°S, 33.6–32.8°S, and 31.1–30.5°S). These features may produce localized recirculations of flow such that total mass transport decreases moving northward, which could present as a slowdown of the current. Indeed, the largest time-mean GLORYS meridional velocities were found at the southern end of the Kermadec Trench. The limited number of Deep Argo trajectories and the different time periods likely also contributed to the discrepancy between Deep Argo and GLORYS velocities.

3.2. Turbulent Mixing

Substantial changes in DWBC θ and salinity properties were observed between Deep Argo profiles upstream (south) and downstream (north) of both the Louisville Seamount Chain collision zone and the Samoan Passage (Figure 2). The highest mean salinities in the DWBC (≥ 34.72) were eroded away as the DWBC exited the Kermadec Trench through the Louisville Seamount Chain collision zone, with such high mean salinities not evident to the north (Figure 2b). The largest θ -salinity differences at the collision zone occurred between roughly 1.2 to 1.7°C (approximately 2,700 to 3,500-dbar), where upstream profiles were substantially saltier at a given temperature than downstream profiles (Figure S2 in Supporting Information S1). This depth range is within the strong northward flow of the DWBC (Figure 5b; Whitworth III et al., 1999). Property changes through the Samoan Passage have been previously documented (e.g., Alford et al., 2013; Voet et al., 2015) and are therefore not discussed here.

The observed θ -salinity changes at the Louisville Seamount Chain collision zone and Samoan Passage imply substantial deep-ocean mixing, which could be due to vertical turbulent diffusivity. In the Louisville Seamount

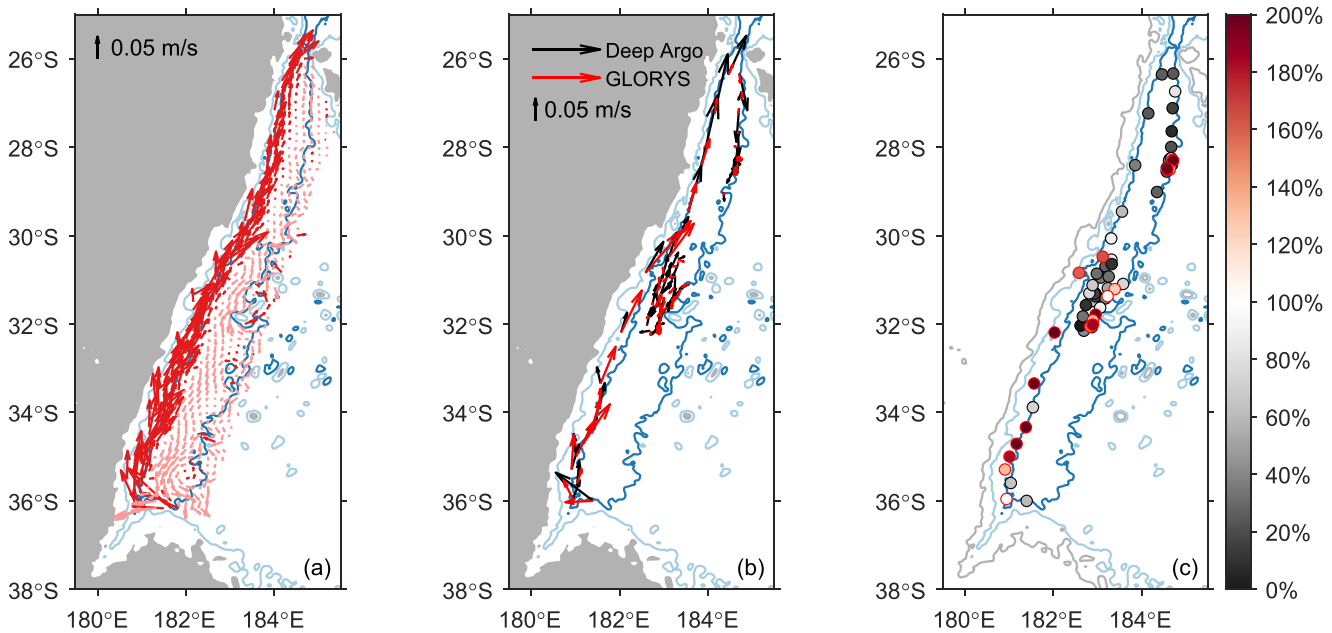


Figure 6. (a) GLORYS time-mean velocity in the Kermadec Trench over 1993–2020 at 5,275-m (plotted at 1/6° resolution). Red arrows are positive meridional velocities, pink arrows are negative. (b) Comparison of Deep Argo trajectory velocity (black arrows) in the Kermadec Trench between 4,500 and 5,500-dbar over 2021–2022 and GLORYS velocity (red arrows) at 5,275-m depth interpolated to the Deep Argo trajectory locations and time-averaged over 1993–2020 for the month in which the corresponding Deep Argo trajectory was obtained. (c) Comparison of the speed (magnitude only) of the Deep Argo trajectories and GLORYS velocities from (b) showing the percent that GLORYS speed is of Deep Argo trajectory speed (red means GLORYS is faster, black means Deep Argo is faster). Bathymetry contours are 4,000-m (gray), 5,000-m (light blue), and 6,000-m (dark blue), with gray shading shallower than 4,000-m.

Chain collision zone, the modeled (Equation 2) evolution of the mean upstream θ -salinity profile due to vertical turbulent diffusivity was rather different from the mean profile observed downstream (Figure S2 in Supporting Information S1). This mismatch between modeled and observed downstream profiles occurred for all spreading scales (λ) and was not dependent on the upper and lower model boundary depths. However, in the Samoan Passage, the modeled evolution due to vertical turbulent diffusivity was exceptionally similar to downstream observations (Figure S1 in Supporting Information S1). A spreading scale of $\lambda = 398$ -m provided the best match between the modeled and mean observed downstream θ -salinity profiles, which, for a distance between mean upstream and downstream profile locations of 504.4-km and a mean Deep Argo trajectory velocity within the Samoan Passage of 0.020 m s^{-1} , resulted in a vertical turbulent diffusivity of $6.2 \times 10^{-3} \text{ m}^2 \text{ s}^{-1}$ (95% confidence interval = 2.9×10^{-3} to $1.00 \times 10^{-2} \text{ m}^2 \text{ s}^{-1}$). Consistent with the model, vertical turbulent diffusivity in the Samoan Passage (below 4,000-dbar) from Deep Argo observations (Equation 3) was estimated to be $1.57 \times 10^{-2} \text{ m}^2 \text{ s}^{-1}$ (7.2×10^{-3} to $2.64 \times 10^{-2} \text{ m}^2 \text{ s}^{-1}$) based on conservation of θ and $6.1 \times 10^{-3} \text{ m}^2 \text{ s}^{-1}$ (2.1×10^{-3} to $2.32 \times 10^{-2} \text{ m}^2 \text{ s}^{-1}$) based on conservation of salinity (Figure 7).

Deep Argo estimates of vertical turbulent diffusivity through the Samoan Passage (from both the numerical model and from direct observations) were also consistent with prior estimates in the Samoan Passage (Figure 7). Using a heat budget approach, Roemmich et al. (1996) estimated diapycnal turbulent diffusivity below 0.7°C to be between 5×10^{-3} and $5 \times 10^{-2} \text{ m}^2 \text{ s}^{-1}$. Waters colder than 0.7°C were not present north of the Samoan Passage (Figure 2a), consistent with these earlier observations, but below 4,750-dbar (the depth closest to 0.7°C in the average profile south of the Samoan Passage) we estimated a vertical turbulent diffusivity of $5.09 \times 10^{-2} \text{ m}^2 \text{ s}^{-1}$ (2.08×10^{-2} to $1.358 \times 10^{-1} \text{ m}^2 \text{ s}^{-1}$) based on conservation of θ (Equation 3). This estimate is at the upper bound of the estimate by Roemmich et al. (1996), but is not unrealistically large for the Samoan Passage (Alford et al., 2013). Voet et al. (2015) used a numerical model (Equation 2) to estimate a vertical turbulent diffusivity of between 3×10^{-3} and $5 \times 10^{-2} \text{ m}^2 \text{ s}^{-1}$ averaged over a depth range comparable to our estimate. Voet et al. (2015) also used Thorpe scales (Dillon, 1982; Thorpe, 1977) to estimate a diapycnal turbulent diffusivity of $6 \times 10^{-3} \text{ m}^2 \text{ s}^{-1}$ below 0.8°C . Implementation of Thorpe scales was not feasible in the present study as Deep Argo profiles often had vertical resolutions of the same magnitude or coarser than the Thorpe length scales found in the Samoan Passage by Voet et al. (2015). However, we estimated vertical turbulent diffusivity below 4,440-

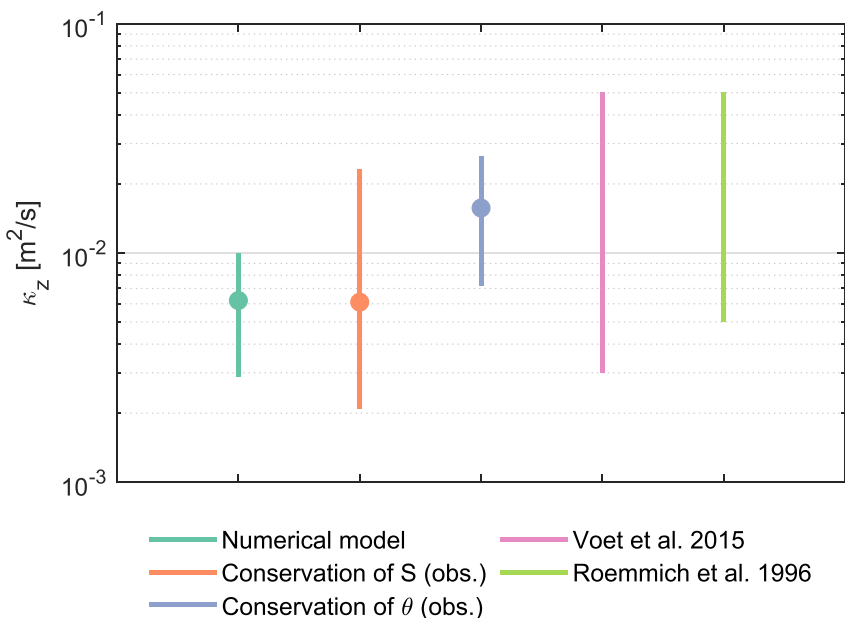


Figure 7. Estimates of vertical turbulent diffusivity (κ_z) through the Samoan Passage from a numerical model applied to upstream Deep Argo observations (aquamarine), and computed from conservation of salinity (orange) and potential temperature (purple) using Deep Argo observations. Filled circles use all Deep Argo data, lines represent bootstrapped 95% confidence intervals. Pink and light-green lines are the range of κ_z estimates through the Samoan Passage from Voet et al. (2015) and Roemmich et al. (1996).

dbar (the depth closest to 0.8°C in the average profile south of the Samoan Passage) to be $8.4 \times 10^{-3} \text{ m}^2 \text{ s}^{-1}$ (3.8×10^{-3} to $1.41 \times 10^{-2} \text{ m}^2 \text{ s}^{-1}$) based on conservation of θ and $4.4 \times 10^{-3} \text{ m}^2 \text{ s}^{-1}$ (1.3×10^{-3} to $2.35 \times 10^{-2} \text{ m}^2 \text{ s}^{-1}$) based on conservation of salinity, consistent with the estimate by Voet et al. (2015).

3.3. Kermadec Trench Seasonality

Deep-ocean seasonal cycles of DH, salinity, and θ between 2,000 and 4,000-dbar were identified from the 2-year time series (2021–2022) of Deep Argo profiles spanning the length of the Kermadec Trench DWBC ($26\text{--}38^\circ\text{S}$). DH (Figure 8a) was negative (i.e., steric contraction) between January–July and positive (i.e., steric expansion) between July–January. The largest signals (at 2,000-dbar relative to 4,000-dbar) of $-0.147 \text{ m}^2 \text{ s}^{-2}$ and $0.129 \text{ m}^2 \text{ s}^{-2}$ occurred in April and November respectively. Salinity (Figure 8b) appeared to be influenced by the vertical movement of the remnant NADW salinity maximum (at approximately 3,500-dbar in the annual average), causing both positive (i.e., saltier) and negative (i.e., fresher) signals to be present each month. The saltiest signal of 0.013 occurred in March and the freshest signal of -0.010 occurred in November, both around 2,900-dbar. Broadly speaking, θ (Figure 8c) was negative (i.e., colder) in February–June and positive (i.e., warmer) in July–January, with the coldest signal of -0.062°C in April at approximately 3,300-dbar and the warmest signal of 0.042°C in December at approximately 3,200-dbar. The onset of the cold signal shifted later with decreasing pressure and there was also a cold signal evident around 2,000-dbar in the midst of the warm months. These two features may be the result of noise in the 2-year time series that was constructed from scattered Deep Argo profiles.

Seasonal cycles observed by Deep Argo were consistent with expected changes due to seasonal heaving of the deep-ocean. Upward motion of the water column would raise isotherms (causing cooling on pressure surfaces) and shift the deep-ocean salinity maximum up (causing salinification at shallower pressures and freshening at deeper pressures). Downward motion of the water column would have the opposite effect (warming on pressure surfaces, freshening at shallower pressures, salinification at deeper pressures). Decomposing the θ seasonal cycle into heave and spice components (Equation 4) confirmed the dominance of heave, with seasonal changes due to heave extremely similar to the total seasonal cycle ($R^2 = 0.89$; Figures 8c–8e). The residual (and therefore error)

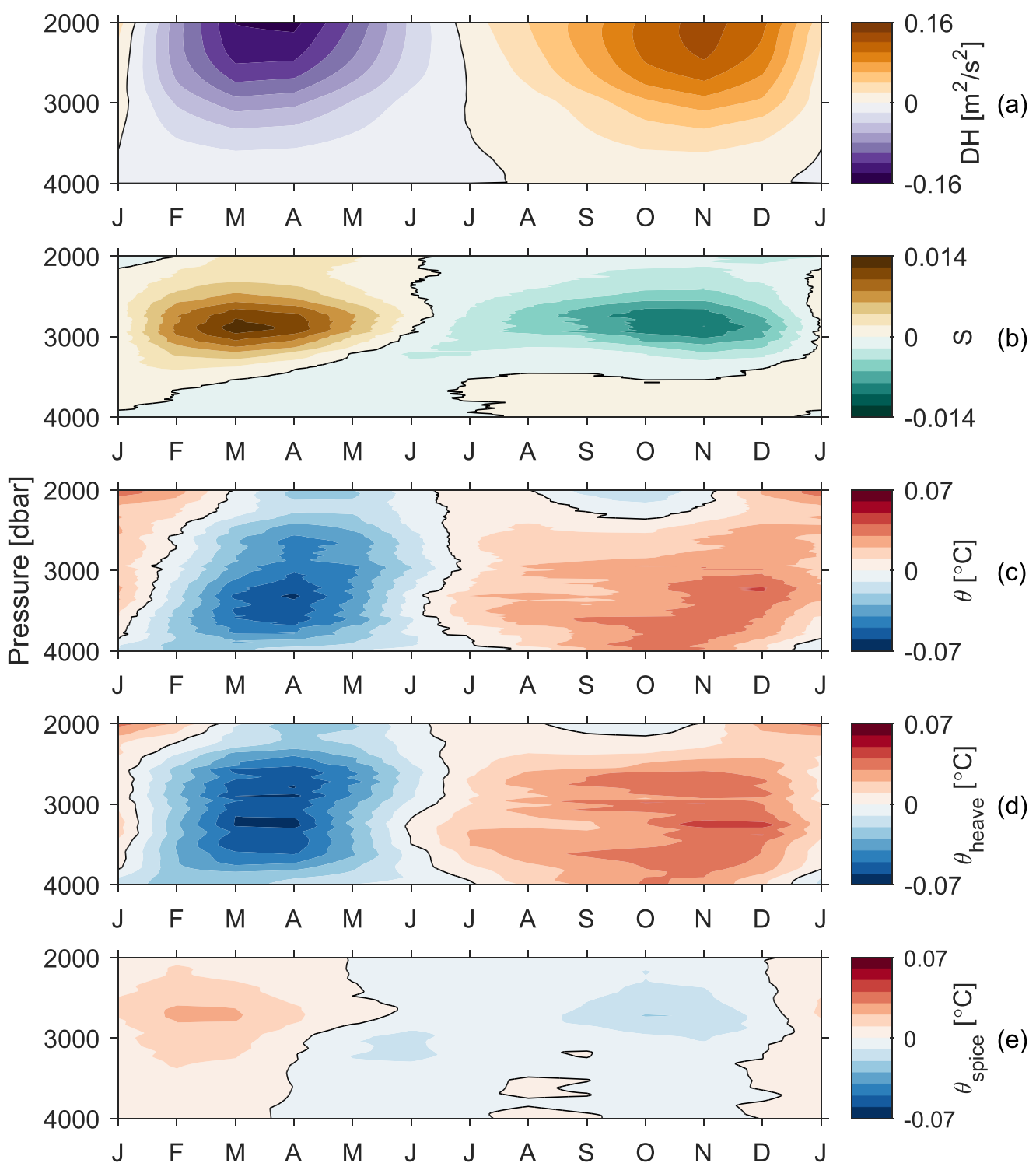


Figure 8. Seasonal cycles between 2,000 and 4,000-dbar from Deep Argo profiles in the Kermadec Trench DWBC (26–38°S) for (a) dynamic height relative to 4,000-dbar (DH), (b) salinity (S), (c) potential temperature (θ), and potential temperature decomposed into (d) heave (θ_{heave}) and (e) spice (θ_{spice}) components. Black line is the 0 contour.

of the decomposition was small ($\text{RMSE} = 0.003^\circ\text{C}$; $R^2 = 0.99$). Applying this heave/spice decomposition to salinity produced the same conclusion.

Changes due to heave are often wind-driven (e.g., Bindoff & McDougall, 1994; Köhl, 2014; Sun et al., 2022), and it has been hypothesized that deep-ocean seasonality in the SWPB interior is driven by Ekman pumping (Zilberman et al., 2020). However, the local Ekman pumping seasonal cycle over the DWBC changes sign between the subtropics and midlatitudes (not shown). This transition occurs between roughly 31–36°S (within the southern half of the Kermadec Trench). The Deep Argo profiles we used to determine the seasonal cycle in the Kermadec Trench DWBC (Figure 8) spanned the entire length of the Kermadec Trench, including this transition region, which complicated the evaluation of Ekman pumping as a possible forcing mechanism. Using Deep Argo profiles to examine a smaller latitude range within the Kermadec Trench DWBC that excluded the transition region was not feasible (but should become possible with sustained Deep Argo observations). Incorporating Deep Argo profiles from the DWBC north of the Kermadec Trench would introduce profiles with different θ -salinity characteristics that could additionally confound results. We therefore used the GLORYS eddy-resolving ocean reanalysis to examine deep-ocean seasonality within the Kermadec Trench DWBC for each of these distinct Ekman pumping regions.

To first validate GLORYS, seasonal cycles of DH, salinity, and θ (over the full 1993–2020 time series) were computed from GLORYS profiles interpolated to the locations of the Deep Argo profiles spanning the full length of the Kermadec Trench DWBC (i.e., the same Deep Argo profiles used for Figure 8). GLORYS DH (Figure 9a) demonstrated steric contraction between December–May and steric expansion between June–December, a difference of 1-month compared to Deep Argo observations. The largest salinity signals in GLORYS (Figure 9b) were observed around 2,000-m, a feature not evident in the Deep Argo seasonal cycle. However, at 2,866-m (a similar depth-level to the largest Deep Argo salinity signals) the saltiest signal occurred in March, at the same time as Deep Argo, and the freshest signal occurred in August, 3-month earlier than Deep Argo. GLORYS θ (Figure 9c) changed sign earlier at shallower depths but, broadly speaking, was colder between December–May and warmer between May–November, a phase difference of 1 to 2-month compared to Deep Argo. This earlier change in sign at shallower depths was likely due to the different seasonal regimes in the northern and southern Kermadec Trench, and largely disappeared when only the northern Kermadec Trench DWBC was considered. Seasonal changes in deep-ocean θ were predominantly due to heave ($R^2 = 0.92$; Figures 9c–9e), as was also found in Deep Argo observations. For all three variables, GLORYS seasonal cycles (Figure 9) were weaker than those observed by Deep Argo (Figure 8). Differences between GLORYS and Deep Argo may be related to the short Deep Argo time series, the uneven and changing distribution of Deep Argo profiles, the different Deep Argo and GLORYS time periods, GLORYS misrepresenting the true seasonal cycle, and/or GLORYS underestimating variability in the deep-ocean. Nevertheless, GLORYS provided a reasonable representation of the observed seasonal cycle phase (Figure 9a) and forcing mechanism (heave) in the Kermadec Trench DWBC. Hence, GLORYS was used to further explore deep-ocean seasonality in the northern (26–30°S) and southern (32–36°S) Kermadec Trench regions that each experienced different Ekman pumping seasonal cycles.

ERA5 Ekman pumping and GLORYS DH, salinity, and θ seasonal cycles were computed over 1993–2020 for the DWBC in northern (Ekman pumping and DH shown in Figure 10; θ and salinity not shown) and southern (not shown) Kermadec Trench regions. The southern Kermadec Trench demonstrated no clear seasonal cycles, as expected given the transitional nature of the Ekman pumping seasonal cycle in this region, and was therefore not investigated further. In the northern Kermadec Trench, the Ekman pumping seasonal cycle (Figure 10a) was positive (i.e., upward) in December–April and negative (i.e., downward) in May–November. DH seasonal changes (steric contraction in December–May, steric expansion in June–November; Figure 10b) were largely consistent with expected changes if Ekman pumping was driving seasonal heaving of the deep-ocean. To confirm this relationship between local Ekman pumping and deep-ocean DH, a coherence analysis (utilizing 6-year segments with a Hanning window applied and 50% overlap) was conducted between the monthly time series of detrended Ekman pumping and DH anomalies over 1993–2020 (Figure S3 in Supporting Information S1). The EOF first-mode principal component was used as a single representative DH time series (accounting for 98% of variance in the 1993–2020 monthly time series of detrended DH anomalies between 2,000 and 4,000-m). For simplicity in interpreting phase, the sign of the principal component was reversed. A statistically significant coherence of 0.83 (exceeding the 95% significance threshold) was found at the annual frequency (Figure 10c). Coherence was not statistically significant at most other frequencies. The phase (Figure 10d) at the annual

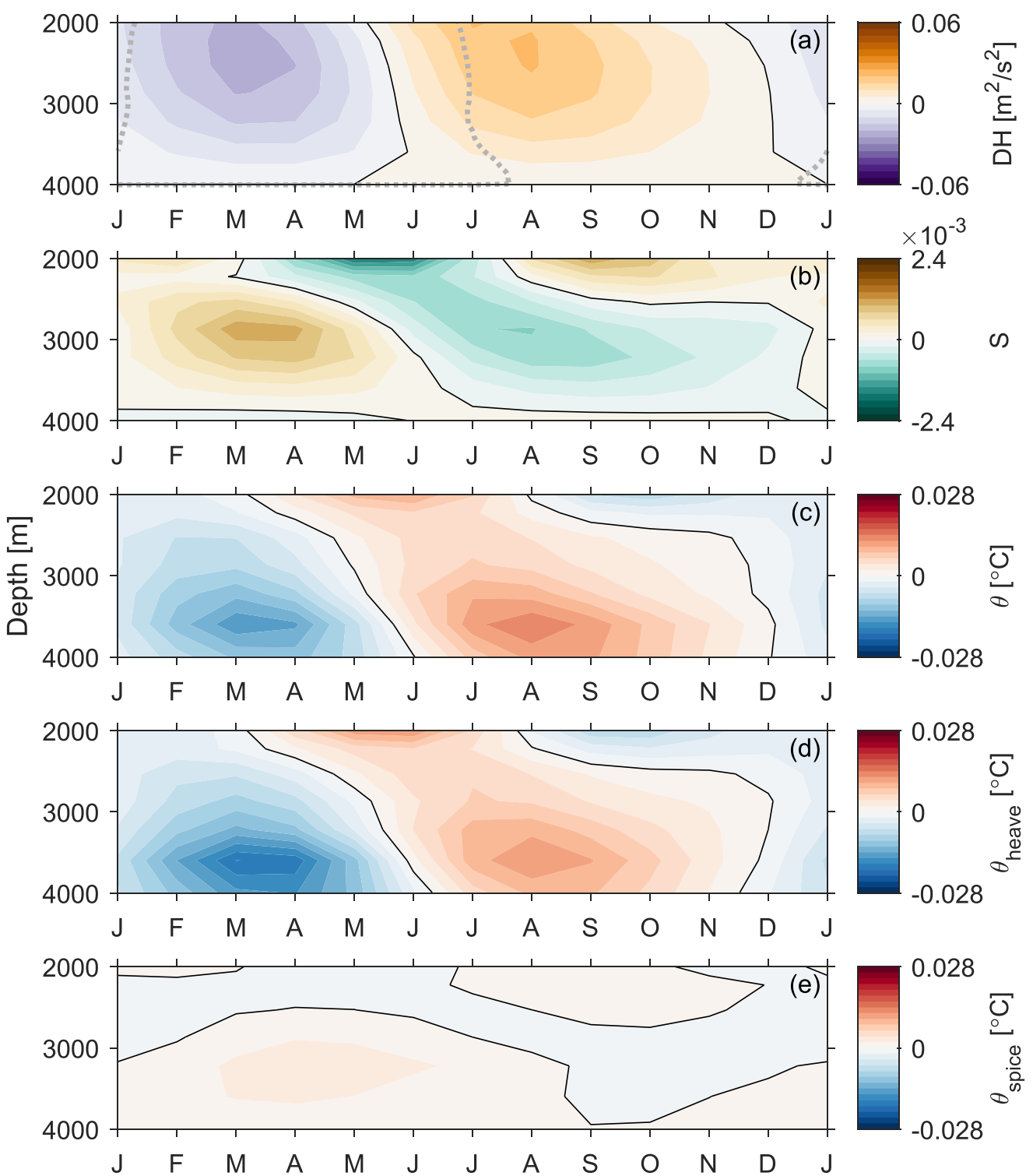


Figure 9. Seasonal cycles between 2,000 and 4,000-m computed from GLORYS (1993–2020) interpolated to the locations of Deep Argo profiles in the Kermadec Trench DWBC (26–38°S) for (a) dynamic height relative to 3,992-m (DH), (b) salinity (S), (c) potential temperature (θ), and potential temperature decomposed into (d) heave (θ_{heave}) and (e) spice (θ_{spice}) components. Black line is the 0 contour. Gray dashed line in (a) is the 0 contour for the 2021–2022 Deep Argo DH seasonal cycle in the Kermadec Trench DWBC (see Figure 8, but note the different color scale).

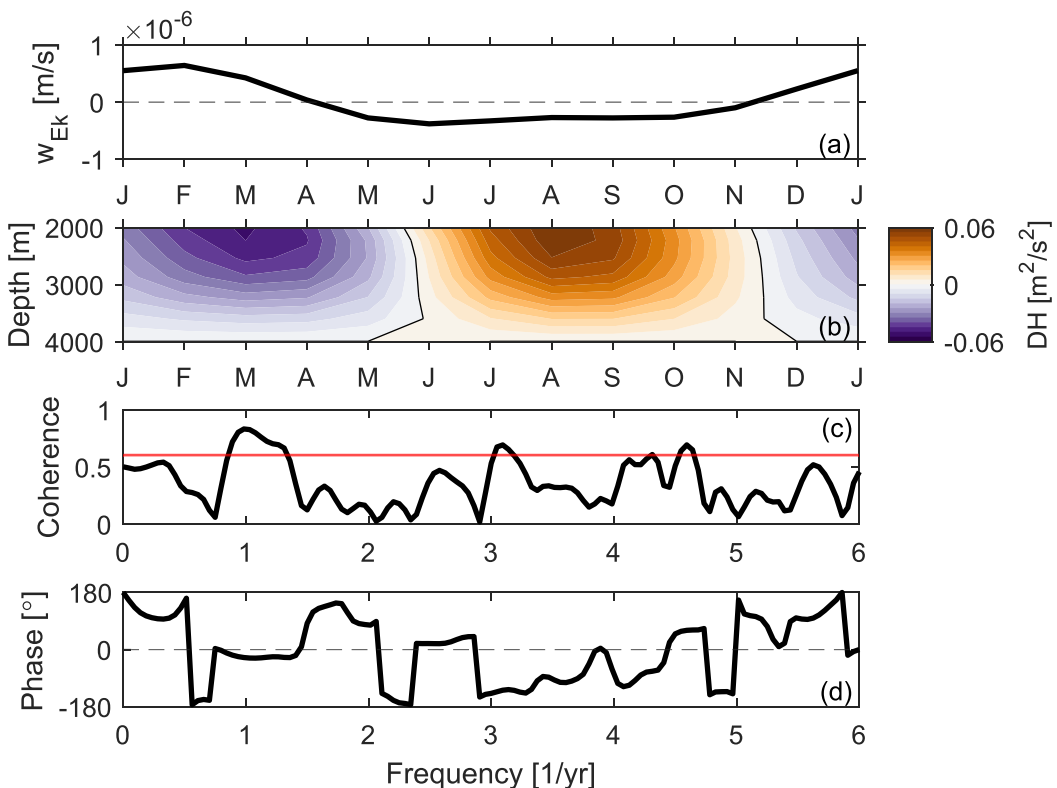


Figure 10. Seasonal cycles in the northern Kermadec Trench DWBC ($26\text{--}30^\circ\text{S}$) for (a) Ekman pumping (w_{EK}) computed from ERA5 and (b) dynamic height relative to 3,992-m (DH) computed from GLORYS (same color scale as Figure 9a). (c) Coherence and (d) phase between 1993–2020 monthly anomalies of w_{EK} and the DH first-mode principal component. Red line is the 95% significance threshold. A negative phase means w_{EK} leads DH.

frequency ($-25 \pm 21^\circ$) indicated that Ekman pumping anomalies led DH anomalies by less than a month. A similar relationship was evident at almost every GLORYS depth level between the surface and 4,000-m (Figure S4 in Supporting Information S1), with coherence between detrended Ekman pumping and DH monthly anomalies over 1993–2020 statistically significant at the annual period for all depths. Phase at the annual period was constant with depth (within uncertainties), except in the near-surface, and indicated that Ekman pumping anomalies led DH anomalies by less than a month.

4. Discussion

The DWBC pathway identified from Deep Argo float trajectories between $5\text{--}40^\circ\text{S}$ over the time period 2016–2022 broadly agrees with, and thus validates, the general pathway previously identified using historical hydrographic observations (Reid, 1986, 1997). However, float trajectories resolved the DWBC pathway in much finer detail than was possible using historical observations. The apparent eddying behavior within the Osbourn Trough does not seem to have been previously identified or characterized, although earlier maps show rather tortuous deep flow pathways at a similar latitude (Reid, 1986, 1997). A hydrographic section along 22°S (intersecting the Osbourn Trough) in 1969 suggested DWBC flow was concentrated alongside the Tonga-Kermadec Ridge and between $168\text{--}165^\circ\text{W}$ (i.e., east of the Deep Argo trajectories in the Osbourn Trough; Warren & Voorhis, 1970). The majority of northward transport across this hydrographic section occurred in the eastern region, although average velocities at 4,200-m were weak ($0.010\text{--}0.017 \text{ m s}^{-1}$; Warren & Voorhis, 1970). These earlier velocities were similar to the average Deep Argo trajectory velocity above 5,500-dbar in the Osbourn Trough ($0.007 \pm 0.013 \text{ m s}^{-1}$, the large uncertainty reflects the large velocity variability). In the low-latitude South Atlantic, the southward-flowing DWBC breaks up into a series of deep anticyclonic eddies around 8°S , with these eddies responsible for all of the DWBC transport across 11°S (Dengler et al., 2004; Schott et al., 2005). We wonder if the situation is similar here, with eddies contributing to DWBC transport across the Osbourn Trough. If so, it may be that the eastern region of DWBC flow measured by Warren and Voorhis (1970) was the northward

velocity of an eddy or series of eddies. An examination of DWBC (and eddy) transport is beyond the scope of this study, with the Deep Argo pilot array not yet robust enough to undertake such work, but we note that 1993–2020 time-mean GLORYS velocities at 5,275-m depth also demonstrated what appeared to be an eddy field within the Osbourn Trough. The breakdown of the southward-flowing South Atlantic DWBC into a series of eddies is caused by upstream instabilities (Dengler et al., 2004), likely barotropic instabilities (Brum et al., 2023). If a similar mechanism is operating in the SWPB, the abrupt change in bathymetry at the Louisville Seamount Chain collision zone could be a possible source of instabilities. Alternatively, the breakdown of coherent DWBC flow may be induced by the deeper and more uniform depth of the Osbourn Trough (typically 5,500 to 6,000-m deep) removing topographic steering constraints.

Deep Argo trajectories also confirmed the occurrence of a cyclonic circulation, consisting of equatorward-flowing DWBC and poleward-flowing recirculation, over the entire Kermadec Trench. The recirculation had previously been inferred based on limited hydrographic and mooring observations (Johnson, 1998). In the early 1990s, three current meters on two moorings at 32.5°S measured poleward velocities within the Kermadec Trench below 3,000-dbar (-0.020 m s^{-1} at 3,970-m, -0.015 m s^{-1} at 5,800-m, -0.010 m s^{-1} at 5,915-m; Whitworth III et al., 1999). Deep Argo trajectory velocities along the eastern side of the Kermadec Trench measured a poleward recirculation with similar magnitude ($-0.021 \pm 0.008 \text{ m s}^{-1}$). The similarity between these independent data sets from different time periods and with different spatial coverage indicates that the tight cyclonic circulation over the Kermadec Trench is a robust feature. Johnson (1998) postulated that cyclonic circulations are common to all deep-ocean trenches with closed $\frac{f}{H}$ contours. A global Deep Argo array could potentially enable determination of whether these cyclonic circulations are indeed a ubiquitous feature of deep-ocean trenches, although such an array has been recommended to use a 1,000-dbar parking pressure consistent with Core Argo (Zilberman, Thierry, et al., 2023) and may therefore not provide deep-ocean trajectories.

Estimates of vertical turbulent diffusivity in the Samoan Passage from a numerical model ($6.2 \times 10^{-3} \text{ m}^2 \text{s}^{-1}$) and from conservation of θ ($1.57 \times 10^{-2} \text{ m}^2 \text{s}^{-1}$) and salinity ($6.1 \times 10^{-3} \text{ m}^2 \text{s}^{-1}$) using direct observations were consistent with prior estimates of vertical turbulent diffusivity in the Samoan Passage (3×10^{-3} to $5 \times 10^{-2} \text{ m}^2 \text{s}^{-1}$; Voet et al., 2015; Roemmich et al., 1996). Deep Argo was therefore able to accurately estimate vertical turbulent diffusivity through the Samoan Passage, a known site of enhanced deep-ocean mixing (Alford et al., 2013; Roemmich et al., 1996; Voet et al., 2015). We expect that Deep Argo observations and this model could be similarly used to evaluate vertical turbulent diffusivity at other sites of enhanced deep-ocean mixing.

Large changes in θ and salinity properties were also observed at the Louisville Seamount Chain collision zone, with the NADW salinity maximum not present north of the collision zone. The Louisville Seamount Chain collision zone had not previously been identified as a site of enhanced deep-ocean mixing, and erosion of the remnant NADW salinity maximum at the collision zone would seem to answer the question posed by Whitworth III et al. (1999) of how this salinity maximum disappears between 32.5°S and the Samoan Passage. However, the modeled evolution of θ and salinity profiles due to vertical turbulent diffusivity within the collision zone was not consistent with the mean profiles observed downstream of the collision zone. As such, the observed change in water mass properties cannot be solely due to vertical turbulent diffusivity. Additional processes, such as horizontal turbulent diffusivity (along isopycnals), must also be important. It is difficult to confidently determine these processes as only two of the Deep Argo floats used in this study had passed through the collision zone.

A global Deep Argo array could reveal other regions of enhanced deep-ocean mixing and thus contribute to improving the representation and distribution of deep-ocean turbulence in climate models. Indeed, Johnson et al. (2022) used Deep Argo descent rates to show that, below 1,000-m, internal wave activity tended to be higher around regions of rougher topography than over the abyssal plains. It is therefore recommended that the vertical resolution of Deep Argo measurements be increased to allow deep-ocean turbulence to be estimated via vertical strain (e.g., Johnson et al., 2022). Efforts are also being made to include microstructure turbulence sensors on Argo floats, including Deep Argo, though this work is yet to be implemented (Roemmich, Alford, et al., 2019).

Seasonal cycles of θ , salinity, and DH between 2,000 and 4,000-dbar were observed by Deep Argo floats in the DWBC along the Kermadec Trench. These seasonal cycles were predominantly due to seasonal heaving of the deep-ocean. Upward heaving raised isotherms (causing cooling on pressure surfaces) and shifted the deep-ocean salinity maximum shallower (causing salinification at shallower pressures and freshening at deeper pressures), with the net result being steric contraction. Downward heaving had the opposite effect. For the DWBC in the

northern Kermadec Trench ($26\text{--}30^\circ\text{S}$), local Ekman pumping anomalies at the surface and GLORYS DH anomalies in the deep-ocean exhibited a statistically significant coherence and were essentially in-phase at the annual period, with downward Ekman pumping anomalies coincident with deep-ocean steric expansion and upward Ekman pumping anomalies coincident with deep-ocean steric contraction. Furthermore, the seasonal steric expansion and contraction, significant coherence, and in-phase relationship were evident throughout the water column (below the seasonal surface mixed-layer and above 4,000-m), as would be expected if local Ekman pumping was driving seasonal heaving. Local Ekman pumping at the surface therefore appears to be the dominant forcing mechanism of the deep-ocean seasonal cycle in the northern Kermadec Trench. However, this relationship may not hold everywhere along the DWBC. For example, the subtropical ($15\text{--}32^\circ\text{S}$) deep-ocean seasonal cycle in the interior of the SWPB (Zilberman et al., 2020) lags local Ekman pumping at the western boundary by 3-month. Continued Deep Argo measurements at the western boundary of the SWPB will enable determination of the deep-ocean seasonal cycle elsewhere along this DWBC.

Other forcing mechanisms seem less likely to be driving the deep-ocean seasonal cycle in the northern Kermadec Trench. Seasonal changes in the production or characteristics of deep-ocean water masses would have to propagate from their high-latitude source regions, and thus changes should be evident in both the southern and northern Kermadec Trench. However, no southern Kermadec Trench deep-ocean seasonal signal was found at the 32.5°S mooring array (Whitworth III et al., 1999), albeit from only a 22-month record, or in the longer 1993–2020 GLORYS output analyzed here. Moore and Wilkin (1998) also discounted deep-water formation processes as a dominant source of variability in this DWBC on seasonal or shorter time scales. Rather, changes at the source regions where these deep-waters are formed tend to drive variability on decadal or longer time scales (Bindoff & McDougall, 1994; Masuda et al., 2010). For example, a reduction in formation of the densest bottom waters over recent decades has caused a downward heave of deep-ocean isotherms (Johnson, 2022; Purkey & Johnson, 2012; Purkey et al., 2019). Propagating features, such as topographic Rossby waves, are another possible forcing mechanism. However, topographic Rossby waves at the western boundary of the SWPB would also travel through the southern Kermadec Trench where no seasonal signal was evident. Instead, topographic Rossby waves are believed to be the dominant source of intra-annual variability in this DWBC at 32.5°S (Moore & Wilkin, 1998; Whitworth III et al., 1999), and in other Southern Hemisphere DWBCs (Fukamachi et al., 2010; Valla et al., 2019).

If we assume there is a consistent Ekman pumping-driven seasonal heaving across the SWPB at the latitude of the northern Kermadec Trench, then a simple potential vorticity or Sverdrup balance argument suggests corresponding seasonal changes in DWBC transport. Vertically integrating the Sverdrup relation through the water column gives the equation for Sverdrup transport:

$$\beta V = f w_{Ek} \quad (5)$$

where β is the Rossby parameter $\left(\frac{\partial f}{\partial y}\right)$ and V is vertically integrated meridional transport (e.g., Cushman-Roisin & Beckers, 2011). This equation suggests that anomalously positive Ekman pumping enhances poleward transport in the interior. To balance this enhanced poleward interior flow, there must be enhanced equatorward transport at the western boundary. The situation reverses for anomalously negative Ekman pumping (i.e., reduced equatorward transport at the western boundary). Indeed, GLORYS meridional velocities at approximately 3,220-m (within the depth range of the observed deep-ocean heaving) demonstrated a velocity seasonal cycle in the northern Kermadec Trench (Figure S5 in Supporting Information S1). DWBC velocities over almost the entire western flank of the northern Kermadec Trench region were significantly stronger in March (northward velocity seasonal maximum) than August (northward velocity seasonal minimum), as the Sverdrup relation argument suggests. However, recirculation velocities on the eastern side of the trench were also stronger in March than August, although only statistically significant over a substantially smaller area. It therefore remains to be seen whether seasonal changes are evident in net DWBC transport. Additionally, this brief examination comes with the caveat that temporal variability in GLORYS deep-ocean velocity has not yet been validated against observations in the Kermadec Trench.

Observing a transport seasonal cycle may be difficult without a long-term time series. The substantial transport variability in this DWBC on shorter time scales (Whitworth III et al., 1999) is likely larger than the seasonal transport signal, similar to that observed in other DWBCs (e.g., Lee et al., 1996; Meinen et al., 2017; Schott

et al., 2005). For an Ekman pumping seasonal amplitude of $6.4 \times 10^{-7} \text{ m s}^{-1}$ (the maximum Ekman pumping seasonal signal for the northern Kermadec Trench) and horizontal distance of 6,000-km (a rough approximation of the SWPB width at 28°S), the interior Sverdrup transport (Equation 5) is -13 Sv . If half of this transport occurs below 2,000-m (barotropic flow in a 4,000-m deep basin), the resulting DWBC transport seasonal signal of 6.5 Sv is clearly overwhelmed by the 1991–1992 DWBC transport standard deviation (11.9 Sv) and range (68.2 Sv) observed below 2,000-m at 32.5°S (Whitworth III et al., 1999).

To the best of our knowledge, this work represents the first time an eddy-resolving ocean reanalysis has been compared against Deep Argo observations in the SWPB. Generally speaking, GLORYS qualitatively reproduced the observed DWBC and recirculation over the Kermadec Trench, although with a bias in velocity magnitude that changed with latitude. GLORYS had previously been found to broadly reproduce deep-ocean velocity in the Philippine Trench (Song et al., 2023) and in the Antarctic Circumpolar Current (Artana et al., 2021). When comparing θ -salinity properties, GLORYS underestimated the deep-ocean salinity maximum and the very coarse vertical resolution of GLORYS in the deep-ocean meant that none of the discrete depth levels were within the core of the observed salinity maximum. GLORYS also had saltier and colder bottom waters than observed by Deep Argo, although this difference could reflect the different time periods. Using Deep Argo profiles in the SWPB, Johnson et al. (2019) observed a mean warming rate below 5,000-dbar of $3 \times 10^{-3} \text{ }^{\circ}\text{C/year}$. Dividing the difference in GLORYS and Deep Argo θ averaged below 5,000-m by this warming rate gives a time scale (12.7-year) that is similar to the time difference between the mean GLORYS and Deep Argo dates (14.8-year). Seasonal cycles observed by Deep Argo were broadly reproduced by GLORYS, with changes predominantly due to heaving in both, but the magnitude of the seasonal signal was much weaker in the reanalysis. Even with these discrepancies, the similarities between Deep Argo observations and GLORYS output in the Kermadec Trench are remarkable given the limited amount of data presently assimilated below 2,000-m. Assimilation of Deep Argo observations into future ocean reanalyses will improve the representation of the deep-ocean, potentially halving deep-ocean temperature and salinity errors (Gasparin et al., 2020). However, until this assimilation occurs, Deep Argo observations provide a means of validating the representation of the deep-ocean in ocean reanalyses and models.

In summary, we have presented new insights into the DWBC of the SWPB using an unprecedented number of deep-ocean observations alongside output from an eddy-resolving ocean reanalysis. The spatial coverage provided by Deep Argo floats has clarified the pathway of this DWBC, including recirculation over the Kermadec Trench and seemingly as an eddy field within the Osbourn Trough. Using changes in θ and salinity along the length of the DWBC we were able to resolve vertical turbulent mixing in the Samoan Passage, and revealed the Louisville Seamount Chain collision zone as a previously unidentified region of enhanced deep-ocean mixing where multiple mixing processes appear to be important. Seasonal heaving of isopycnals was evident in the DWBC and, in the northern Kermadec Trench, was found to be driven by local winds. However, this work only examined one Southern Hemisphere DWBC. We hypothesize that enhanced deep-ocean mixing at bathymetric choke-points and wind-driven seasonal heaving will also be present in other DWBCs. Even so, limited DWBC observations mean these characteristics may not be identifiable until a global deep-ocean observing system, such as a mature Deep Argo array, is achieved.

Data Availability Statement

Argo data is collected and made available by the International Argo Program and the national programs that contribute to it (Argo, 2024). The Scripps Argo Trajectory-Based Velocity Product is available from the UC San Diego Library at <https://doi.org/10.6075/J0NK3F7V> (Zilberman, Scanderbeg, et al., 2023b). GLORYS data is available from the EU Copernicus Marine Service at <https://doi.org/10.48670/moi-00021> (CMEMS, 2018). ERA5 data is available from the Copernicus Climate Change Service at <https://doi.org/10.24381/cds.f17050d7> (Hersbach et al., 2023). WOCE current meter data was downloaded from NOAA National Centers for Environmental Information (<https://www.nodc.noaa.gov/archive/arc0001/0000649/1.1/data/0-data/disk2/cmdac/explist.htm>). Bathymetry data was from the ETOPO1 data set which is made available by NOAA National Centers for Environmental Information at <https://doi.org/10.7289/V5C8276M> (NOAA, 2009). Colourmaps are from BrewerMap (<https://github.com/DrosteEffect/BrewerMap>). This work utilised the Gibbs-SeaWater Oceanographic Toolbox (McDougall & Barker, 2011). The Deep Argo profiles and trajectories used in this study have been made permanently and publicly available at <https://doi.org/10.5281/zenodo.10791519> (Chandler, 2024). Monthly time series and seasonal cycles of potential temperature, salinity, and dynamic height from the spatially averaged Deep

Argo profiles within the Kermadec Trench DWBC have also been made permanently and publicly available at <https://doi.org/10.5281/zenodo.10791519> (Chandler, 2024).

Acknowledgments

We would like to acknowledge Phil Sutton, Denise Fernandez, Matt Walkington and the crews of the R/V Kaharoa and R/V Tangaroa for their work in deploying the Deep Argo floats used in this study, John Gilson for conducting the delayed-mode quality control of these Deep Argo floats, Megan Scanderbeg for maintaining the Scripps Argo Trajectory-Based Velocity Product, and Gunnar Voet for providing the code for the numerical model. We also thank two anonymous reviewers for their time and feedback. MC and NZ received support from NOPP (NOAA grant NA18OAR0110434). MC, NZ, and JS received support from the NOAA Global Ocean Monitoring and Observing Program through Award NA20OAR4320278. NZ received support from NSF (OCE-2242742).

References

- Alford, M. H., Girton, J. B., Voet, G., Carter, G. S., Mickett, J. B., & Klymak, J. M. (2013). Turbulent mixing and hydraulic control of abyssal water in the Samoan Passage. *Geophysical Research Letters*, 40(17), 4668–4674. <https://doi.org/10.1029/grl.50684>
- Argo. (2024). Argo float data and metadata from global data Assembly Centre (Argo GDAC) [Dataset]. SEANOE. <https://doi.org/10.17882/42182>
- Artana, C., Ferrari, R., Brécaud, C., Lellouche, J.-M., Garric, G., Sennéchal, N., et al. (2021). Twenty-five years of Mercator ocean reanalysis GLORYS12 at Drake Passage: Velocity assessment and total volume transport. *Advances in Space Research*, 68(2), 447–466. <https://doi.org/10.1016/j.asr.2019.11.033>
- Bindoff, N. L., & McDougall, T. J. (1994). Diagnosing climate change and ocean ventilation using hydrographic data. *Journal of Physical Oceanography*, 24(6), 1137–1152. [https://doi.org/10.1175/1520-0485\(1994\)024\(1137:DCCAOV\)2.0.CO;2](https://doi.org/10.1175/1520-0485(1994)024(1137:DCCAOV)2.0.CO;2)
- Brum, A. L., de Azevedo, J. L. L., & Dengler, M. (2023). Energetics of eddy-mean flow interactions in the deep western boundary current off the northeastern coast of Brazil. *Deep Sea Research Part I: Oceanographic Research Papers*, 193, 103965. <https://doi.org/10.1016/j.dsr.2023.103965>
- Chandler, M. (2024). Data in support of the deep western boundary current of the Southwest Pacific Basin: Insights from deep Argo [Dataset]. Zenodo. <https://doi.org/10.5281/zenodo.1079159>
- CMEMS. (2018). Global Ocean Physics reanalysis [Dataset]. Copernicus Marine Service Information Marine Data Store. <https://doi.org/10.48670/MOI-00021>
- Cushman-Roisin, B., & Beckers, J.-M. (2011). *Introduction to geophysical fluid dynamics: Physical and numerical aspects* (2nd ed.), Academic Press.
- Dengler, M., Schott, F. A., Eden, C., Brandt, P., Fischer, J., & Zantopp, R. J. (2004). Break-up of the Atlantic deep western boundary current into eddies at 8°S. *Nature*, 432(7020), 1018–1020. <https://doi.org/10.1038/nature03134>
- Desbruyères, D. G., Bravo, E. P., Thierry, V., Mercier, H., Lherminier, P., Cabanes, C., et al. (2022). Warming-to-Cooling reversal of overflow-derived water masses in the Irminger sea during 2002–2021. *Geophysical Research Letters*, 49(10), e2022GL098057. <https://doi.org/10.1029/2022GL098057>
- Desbruyères, D. G., Purkey, S. G., McDonagh, E. L., Johnson, G. C., & King, B. A. (2016). Deep and abyssal ocean warming from 35 years of repeat hydrography. *Geophysical Research Letters*, 43(19), 10356–10365. <https://doi.org/10.1002/2016GL070413>
- Dillon, T. M. (1982). Vertical overturns: A comparison of Thorpe and Ozmidov length scales. *Journal of Geophysical Research*, 87(C12), 9601–9613. <https://doi.org/10.1029/JC087C12p09601>
- Ffield, A., & Gordon, A. L. (1992). Vertical mixing in the Indonesian thermocline. *Journal of Physical Oceanography*, 22(2), 184–195. [https://doi.org/10.1175/1520-0485\(1992\)022\(0184:VMITIT\)2.0.CO;2](https://doi.org/10.1175/1520-0485(1992)022(0184:VMITIT)2.0.CO;2)
- Foppert, A., Rintoul, S. R., Purkey, S. G., Zilberman, N., Kobayashi, T., Sallée, J.-B., et al. (2021). Deep Argo reveals bottom water properties and pathways in the Australian-Antarctic basin. *Journal of Geophysical Research: Oceans*, 126(12), e2021JC017935. <https://doi.org/10.1029/2021JC017935>
- Fukamachi, Y., Rintoul, S. R., Church, J. A., Aoki, S., Sokolov, S., Rosenberg, M. A., & Wakatsuchi, M. (2010). Strong export of Antarctic bottom water east of the Kerguelen plateau. *Nature Geoscience*, 3(5), 327–331. <https://doi.org/10.1038/ngeo842>
- Gasparin, F., Hamon, M., Rémy, E., & Traon, P.-Y. L. (2020). How deep Argo will improve the deep ocean in an ocean reanalysis. *Journal of Climate*, 33(1), 77–94. <https://doi.org/10.1175/JCLI-D-19-0208.1>
- Gunn, K. L., Rintoul, S. R., England, M. H., & Bowen, M. M. (2023). Recent reduced abyssal overturning and ventilation in the Australian Antarctic Basin. *Nature Climate Change*, 13(6), 1–8. <https://doi.org/10.1038/s41558-023-01667-8>
- Häkkinen, S., Rhines, P. B., & Worthen, D. L. (2015). Heat content variability in the North Atlantic Ocean in ocean reanalyses. *Geophysical Research Letters*, 42(8), 2901–2909. <https://doi.org/10.1002/2015GL063299>
- Hersbach, H., Bell, B., Berrisford, P., Biavati, G., Horányi, A., Muñoz Sabater, J., et al. (2023). ERA5 monthly averaged data on single levels from 1940 to present [Dataset]. Copernicus Climate Change Service Climate Data Store. <https://doi.org/10.24381/CDS.F17050D7>
- Hersbach, H., Bell, B., Berrisford, P., Hirahara, S., Horányi, A., Muñoz-Sabater, J., et al. (2020). The ERA5 global reanalysis. *Quarterly Journal of the Royal Meteorological Society*, 146(730), 1999–2049. <https://doi.org/10.1002/qj.3803>
- Johnson, G. C. (1998). Deep water properties, velocities, and dynamics over ocean trenches. *Journal of Marine Research*, 56(2), 329–347. <https://doi.org/10.1357/002224098321822339>
- Johnson, G. C. (2008). Quantifying Antarctic bottom water and North Atlantic deep water volumes. *Journal of Geophysical Research*, 113(C5). <https://doi.org/10.1029/2007JC004477>
- Johnson, G. C. (2022). Antarctic bottom water warming and circulation slowdown in the Argentine basin from analyses of deep Argo and historical shipboard temperature data. *Geophysical Research Letters*, 49(18), e2022GL100526. <https://doi.org/10.1029/2022GL100526>
- Johnson, G. C., Cadot, C., Lyman, J. M., McTaggart, K. E., & Steffen, E. L. (2020). Antarctic bottom water warming in the Brazil basin: 1990s through 2020, from WOCE to deep Argo. *Geophysical Research Letters*, 47(18), e2020GL089191. <https://doi.org/10.1029/2020GL089191>
- Johnson, G. C., Purkey, S. G., Zilberman, N. V., & Roemmich, D. (2019). Deep Argo quantifies bottom water warming rates in the Southwest Pacific Basin. *Geophysical Research Letters*, 46(5), 2662–2669. <https://doi.org/10.1029/2018GL081685>
- Johnson, G. C., Whalen, C. B., Purkey, S. G., & Zilberman, N. (2022). Serendipitous internal wave signals in deep Argo data. *Geophysical Research Letters*, 49(7), e2022GL097900. <https://doi.org/10.1029/2022GL097900>
- Köhrl, A. (2014). Detecting processes contributing to interannual Halosteric and Thermosteric sea level variability. *Journal of Climate*, 27(6), 2417–2426. <https://doi.org/10.1175/JCLI-D-13-00412.1>
- Kouketsu, S., Doi, T., Kawano, T., Masuda, S., Sugiura, N., Sasaki, Y., et al. (2011). Deep ocean heat content changes estimated from observation and reanalysis product and their influence on sea level change. *Journal of Geophysical Research*, 116(C3), C03012. <https://doi.org/10.1029/2010JC006464>
- Lee, T. N., Johns, W. E., Zantopp, R. J., & Fillenbaum, E. R. (1996). Moored observations of western boundary current variability and thermohaline circulation at 26.5° in the subtropical North Atlantic. *Journal of Physical Oceanography*, 26(6), 962–983. [https://doi.org/10.1175/1520-0485\(1996\)026\(0962:MOOWBC\)2.0.CO;2](https://doi.org/10.1175/1520-0485(1996)026(0962:MOOWBC)2.0.CO;2)
- Lellouche, J.-M., Greiner, E., Bourdallé-Badie, R., Garric, G., Melet, A., Drévillon, M., et al. (2021). The Copernicus global 1/12° oceanic and sea ice GLORYS12 reanalysis. *Frontiers in Earth Science*, 9. <https://doi.org/10.3389/feart.2021.698876>

- Lellouche, J.-M., Greiner, E., Le Galloudec, O., Garric, G., Regnier, C., Drevillon, M., et al. (2018). Recent updates to the Copernicus Marine Service global ocean monitoring and forecasting real-time 1/12° high-resolution system. *Ocean Science*, 14(5), 1093–1126. <https://doi.org/10.5194/os-14-1093-2018>
- Masuda, S., Awaji, T., Sugiura, N., Matthews, J. P., Toyoda, T., Kawai, Y., et al. (2010). Simulated rapid warming of abyssal North Pacific waters. *Science*, 329(5989), 319–322. <https://doi.org/10.1126/science.1188703>
- McDougall, T. J., & Barker, P. M. (2011). Getting started with TEOS-10 and the Gibbs Seawater (GSW) oceanographic Toolbox. *Battery Point, Tas: SCOR/IAPSO WG127*.
- Meinen, C. S., Garzoli, S. L., Perez, R. C., Campos, E., Piola, A. R., Chidichimo, M. P., et al. (2017). Characteristics and causes of deep western boundary current transport variability at 34.5°S during 2009–2014. *Ocean Science*, 13(1), 175–194. <https://doi.org/10.5194/os-13-175-2017>
- Moore, M. I., & Wilkin, J. L. (1998). Variability in the South Pacific deep western boundary current from current meter observations and a high-resolution global model. *Journal of Geophysical Research*, 103(C3), 5439–5457. <https://doi.org/10.1029/97JC03207>
- Munk, W. H. (1966). Abyssal recipes. *Deep-Sea Research and Oceanographic Abstracts*, 13(4), 707–730. [https://doi.org/10.1016/0011-7471\(66\)90602-4](https://doi.org/10.1016/0011-7471(66)90602-4)
- NOAA. (2009).ETOPO1 1 Arc-minute global relief model [Dataset]. NOAA National Centers for Environmental Information. <https://doi.org/10.7289/V5C8276M>
- Petit, T., Thierry, V., & Mercier, H. (2022). Deep through-flow in the bright fracture zone. *Ocean Science*, 18(4), 1055–1071. <https://doi.org/10.5194/os-18-1055-2022>
- Purkey, S. G., & Johnson, G. C. (2010). Warming of global abyssal and deep southern ocean waters between the 1990s and 2000s: Contributions to global heat and sea level rise budgets. *Journal of Climate*, 23(23), 6336–6351. <https://doi.org/10.1175/2010JCLI3682.1>
- Purkey, S. G., & Johnson, G. C. (2012). Global contraction of Antarctic bottom water between the 1980s and 2000s. *Journal of Climate*, 25(17), 5830–5844. <https://doi.org/10.1175/JCLI-D-11-00612.1>
- Purkey, S. G., & Johnson, G. C. (2013). Antarctic bottom water warming and freshening: Contributions to sea level rise, ocean freshwater budgets, and global heat gain. *Journal of Climate*, 26(16), 6105–6122. <https://doi.org/10.1175/JCLI-D-12-00834.1>
- Purkey, S. G., Johnson, G. C., Talley, L. D., Sloyan, B. M., Wijffels, S. E., Smethie, W., et al. (2019). Unabated bottom water warming and freshening in the South Pacific ocean. *Journal of Geophysical Research: Oceans*, 124(3), 1778–1794. <https://doi.org/10.1029/2018JC014775>
- Racapé, V., Thierry, V., Mercier, H., & Cabanes, C. (2019). ISOW spreading and mixing as revealed by deep-Argo floats launched in the Charlie-Gibbs fracture zone. *Journal of Geophysical Research: Oceans*, 124(10), 6787–6808. <https://doi.org/10.1029/2019JC015040>
- Reid, J. L. (1986). On the total geostrophic circulation of the South Pacific Ocean: Flow patterns, tracers and transports. *Progress in Oceanography*, 16(1), 1–61. [https://doi.org/10.1016/0079-6611\(86\)90036-4](https://doi.org/10.1016/0079-6611(86)90036-4)
- Reid, J. L. (1997). On the total geostrophic circulation of the Pacific Ocean: Flow patterns, tracers, and transports. *Progress in Oceanography*, 39(4), 263–352. [https://doi.org/10.1016/S0079-6611\(97\)00012-8](https://doi.org/10.1016/S0079-6611(97)00012-8)
- Roemmich, D., Alford, M. H., Claustre, H., Johnson, K., King, B., Moum, J., et al. (2019a). On the future of Argo: A global, full-depth, multidisciplinary array. *Frontiers in Marine Science*, 6. <https://doi.org/10.3389/fmars.2019.00439>
- Roemmich, D., Hautala, S., & Rudnick, D. (1996). Northward abyssal transport through the Samoan passage and adjacent regions. *Journal of Geophysical Research*, 101(C6), 14039–14055. <https://doi.org/10.1029/96JC00797>
- Roemmich, D., Sherman, J. T., Davis, R. E., Grindley, K., McClune, M., Parker, C. J., et al. (2019b). Deep SOLO: A full-depth profiling float for the Argo program. *Journal of Atmospheric and Oceanic Technology*, 36(10), 1967–1981. <https://doi.org/10.1175/JTECH-D-19-0066.1>
- Roemmich, D., Talley, L., Zilberman, N., Osborne, E., Johnson, K., Barbero, L., et al. (2021). The technological, scientific, and sociological revolution of global subsurface ocean observing. *Oceanography*, 34(4), 2–8. <https://doi.org/10.5670/oceanog.2021.supplement.02-02>
- Rudnick, D. L. (1997). Direct velocity measurements in the Samoan Passage. *Journal of Geophysical Research*, 102(C2), 3293–3302. <https://doi.org/10.1029/96JC03286>
- Salmon, R. (1998). *Lectures on geophysical fluid dynamics*. Oxford University Press.
- Schott, F. A., Dengler, M., Zantopp, R., Stramma, L., Fischer, J., & Brandt, P. (2005). The shallow and deep western boundary circulation of the South Atlantic at 5°–11°S. *Journal of Physical Oceanography*, 35(11), 2031–2053. <https://doi.org/10.1175/JPO2813.1>
- Sloyan, B. M., Wanninkhof, R., Kramp, M., Johnson, G. C., Talley, L. D., Tanhua, T., et al. (2019). The Global Ocean Ship-based Hydrographic Investigations Program (GO-SHIP): A platform for integrated multidisciplinary ocean science. *Frontiers in Marine Science*, 6. <https://doi.org/10.3389/fmars.2019.00445>
- Sloyan, B. M., Wijffels, S. E., Tilbrook, B., Katsumata, K., Murata, A., & Macdonald, A. M. (2013). Deep Ocean changes near the western boundary of the South Pacific Ocean. *Journal of Physical Oceanography*, 43(10), 2132–2141. <https://doi.org/10.1175/JPO-D-12-0182.1>
- Song, H., Zhu, X.-H., Zhu, Z.-N., Chae, J.-Y., Jeon, C., Kim, D.-G., et al. (2023). Seasonal variability of the deep western boundary current in the Philippine Sea. *Journal of Marine Science and Engineering*, 11(7), 1290. <https://doi.org/10.3390/jmse11071290>
- Stommel, H., & Arons, A. B. (1959a). On the abyssal circulation of the world ocean — II. An idealized model of the circulation pattern and amplitude in oceanic basins. *Deep-Sea Research*, 6, 217–233. [https://doi.org/10.1016/0146-6313\(59\)90075-9](https://doi.org/10.1016/0146-6313(59)90075-9)
- Stommel, H., & Arons, A. B. (1959b). On the abyssal circulation of the world ocean—I. Stationary planetary flow patterns on a sphere. *Deep-Sea Research*, 6, 140–154. [https://doi.org/10.1016/0146-6313\(59\)90065-6](https://doi.org/10.1016/0146-6313(59)90065-6)
- Sun, J., Zhang, L., & Hu, D. (2022). Decadal and long-term variability of sea level in the southwestern Pacific during 1948–2018. *Geophysical Research Letters*, 49(11), e2022GL098747. <https://doi.org/10.1029/2022GL098747>
- Talley, L. D. (2013). Closure of the global overturning circulation through the Indian, Pacific, and southern oceans: Schematics and transports. *Oceanography*, 26(1), 80–97. <https://doi.org/10.5670/oceanog.2013.07>
- Thomas, G., Purkey, S. G., Roemmich, D., Foppert, A., & Rintoul, S. R. (2020). Spatial variability of Antarctic bottom water in the Australian Antarctic basin from 2018–2020 captured by deep Argo. *Geophysical Research Letters*, 47(23), e2020GL089467. <https://doi.org/10.1029/2020GL089467>
- Thorpe, S. A. (1977). Turbulence and mixing in a Scottish Loch. *Philosophical Transactions of the Royal Society of London—Series A: Mathematical and Physical Sciences*, 286(1334), 125–181. <https://doi.org/10.1088/rsta.1977.0112>
- Toole, J. M., Schmitt, R. W., & Polzin, K. L. (1994). Estimates of Diapycnal mixing in the abyssal ocean. *Science*, 264(5162), 1120–1123. <https://doi.org/10.1126/science.264.5162.1120>
- Valla, D., Piola, A. R., Meinen, C. S., & Campos, E. (2019). Abyssal transport variations in the Southwest South Atlantic: First insights from a long-term observation array at 34.5°S. *Geophysical Research Letters*, 46(12), 6699–6705. <https://doi.org/10.1029/2019GL082740>
- Voet, G., Alford, M. H., Girton, J. B., Carter, G. S., Mickett, J. B., & Klymak, J. M. (2016). Warming and weakening of the abyssal flow through Samoan passage. *Journal of Physical Oceanography*, 46(8), 2389–2401. <https://doi.org/10.1175/JPO-D-16-0063.1>
- Voet, G., Girton, J. B., Alford, M. H., Carter, G. S., Klymak, J. M., & Mickett, J. B. (2015). Pathways, volume transport, and mixing of abyssal water in the Samoan passage. *Journal of Physical Oceanography*, 45(2), 562–588. <https://doi.org/10.1175/JPO-D-14-0096.1>

- Warren, B. A. (1973). Transpacific hydrographic sections at Lats. 43°S and 28°S: The SCORPIO expedition—II. Deep water. *Deep-Sea Research and Oceanographic Abstracts*, 20(1), 9–38. [https://doi.org/10.1016/0011-7471\(73\)90040-5](https://doi.org/10.1016/0011-7471(73)90040-5)
- Warren, B. A. (1981). Transindian hydrographic section at Lat. 18°S: Property distributions and circulation in the South Indian ocean. *Deep-Sea Research, Part A: Oceanographic Research Papers*, 28(8), 759. [https://doi.org/10.1016/S0198-0149\(81\)80001-5](https://doi.org/10.1016/S0198-0149(81)80001-5)
- Warren, B. A., & Voorhis, A. D. (1970). Velocity measurements in the deep western boundary current of the South Pacific. *Nature*, 228(5274), 849–850. <https://doi.org/10.1038/228849b0>
- Whitworth, T. III, Nowlin, W. D. Jr., Pillsbury, R. D., Moore, M. I., & Weiss, R. F. (1991). Observations of the Antarctic circumpolar current and deep boundary current in the Southwest Atlantic. *Journal of Geophysical Research*, 96(C8), 15105–15118. <https://doi.org/10.1029/91JC01319>
- Whitworth, T. III, Warren, B. A., Nowlin, J. W. D., Rutz, S. B., Pillsbury, R. D., & Moore, M. I. (1999). On the deep western-boundary current in the Southwest Pacific Basin. *Progress in Oceanography*, 43(1), 1–54. [https://doi.org/10.1016/S0079-6611\(99\)00005-1](https://doi.org/10.1016/S0079-6611(99)00005-1)
- Wijffels, S. E., Toole, J. M., & Davis, R. (2001). Revisiting the South Pacific subtropical circulation: A synthesis of world ocean circulation experiment observations along 32°S. *Journal of Geophysical Research*, 106(C9), 19481–19513. <https://doi.org/10.1029/1999JC000118>
- Wong, A., Keeley, R., & Carval, T., & Argo Data Management Team. (2022). Argo quality control manual for CTD and trajectory data. <https://doi.org/10.13155/33951>
- Zilberman, N., Roemmich, D. H., & Gilson, J. (2020). Deep-Ocean circulation in the Southwest Pacific Ocean interior: Estimates of the mean flow and variability using deep Argo data. *Geophysical Research Letters*, 47(13), e2020GL088342. <https://doi.org/10.1029/2020GL088342>
- Zilberman, N. V., Scanderbeg, M., Gray, A. R., & Oke, P. R. (2023a). Scripps Argo trajectory-based velocity product: Global estimates of absolute velocity derived from core, biogeochemical, and deep Argo float trajectories at parking depth. *Journal of Atmospheric and Oceanic Technology*, 40(3), 361–374. <https://doi.org/10.1175/JTECH-D-22-0065.1>
- Zilberman, N. V., Scanderbeg, M. C., Gray, A. R., & Oke, P. R. (2023b). Scripps Argo trajectory-based velocity product 2001–01 to 2022–12 [Dataset]. UC San Diego Library Digital Collections. <https://doi.org/10.6075/J0NK3F7V>
- Zilberman, N. V., Thierry, V., King, B., Alford, M., André, X., Balem, K., et al. (2023). Observing the full ocean volume using Deep Argo floats. *Frontiers in Marine Science*, 10. <https://doi.org/10.3389/fmars.2023.1287867>